Neurobiology of Disease 152 (2021) 105275

Contents lists available at ScienceDirect

Neurobiology of Disease

journal homepage: www.elsevier.com/locate/ynbdi

Increased responsiveness at the cerebellar input stage in the PRRT2 knockout model of paroxysmal kinesigenic dyskinesia

Francesca Binda [a,1,2], Pierluigi Valente [b,c,1], Antonella Marte [b], Pietro Baldelli [b,c], Fabio Benfenati [a,c,*]

[a] Center for Synaptic Neuroscience and Technology, Istituto Italiano di Tecnologia, Largo Rosanna Benzi 10, 16132 Genova, Italy
[b] Department of Experimental Medicine, University of Genova, Viale Benedetto XV, 3, 16132 Genova, Italy
[c] IRCCS, Ospedale Policlinico San Martino, Largo Rosanna Benzi 10, 16132 Genova, Italy

ARTICLE INFO

Keywords:
PRRT2
Na^+ channels
Intrinsic excitability
Cerebellar granules

ABSTRACT

PRoline-Rich Transmembrane protein-2 (PRRT2) is a recently described neuron-specific type-2 integral membrane protein with a large cytosolic N-terminal domain that distributes in presynaptic and axonal domains where it interacts with several presynaptic proteins and voltage-gated Na^+ channels. Several PRRT2 mutations are the main cause of a wide and heterogeneous spectrum of paroxysmal disorders with a loss-of-function patho-mechanism. The highest expression levels of PRRT2 in brain occurs in cerebellar granule cells (GCs) and cerebellar dysfunctions participate in the dyskinetic phenotype of PRRT2 knockout (KO) mice. We have investigated the effects of PRRT2 deficiency on the intrinsic excitability of GCs and the input-output relationships at the mossy fiber-GC synapses. We show that PRRT2 KO primary GCs display increased expression of Na^+ channels, increased amplitude of Na^+ currents and increased length of the axon initial segment, leading to an overall enhancement of intrinsic excitability. In acute PRRT2 KO cerebellar slices, GCs were more prone to action potential discharge in response to mossy fiber activation and exhibited an enhancement of transient and persistent Na^+ currents, in the absence of changes at the mossy fiber-GC synapses. The results support a key role of PRRT2 expressed in GCs in the physiological regulation of the excitatory input to the cerebellum and are consistent with a major role of a cerebellar dysfunction in the pathogenesis of the PRRT2-linked paroxysmal pathologies.

1. Introduction

Mutations in the PRoline-Rich Transmembrane protein-2 (PRRT2) were found to be the main cause of a wide and heterogeneous spectrum of paroxysmal disorders including paroxysmal kinesigenic dyskinesia (PKD), benign familial infantile epilepsy, PKD with infantile convulsions, episodic ataxia and hemiplegic migraine. Over seventy distinct mutations have been reported in association with these paroxysmal disorders and 78% of cases showed the same frameshift mutation (c.649dupC) that leads to a premature stop codon (Heron and Dibbens, 2013; Ebrahimi-Fakhari et al., 2015; Valtorta et al., 2016). Most of these mutations lead to unstable mRNA or a non-functional truncated protein that fails to be targeted or becomes degraded, supporting a loss-of-function patho-mechanism (Chen et al., 2011; Lee et al., 2012; Liu et al., 2016; Tsai et al., 2019).

PRRT2 is a recently described neuron-specific type-2 integral membrane protein with a large cytosolic N-terminal domain (Rossi et al., 2016) that distributes in presynaptic and axonal domains, where it interacts with several presynaptic proteins involved in synaptic transmission including SNARE proteins, synaptotagmin and the actin cytoskeleton (Valente et al., 2016a; Coleman et al., 2018; Savino et al., 2020). Knockdown of PRRT2 sharply decreases the Ca^{2+}-sensitivity of the release machinery, leading to an impairment of basal synaptic transmission and a dramatic increase of facilitation of excitatory

Abbreviations: AIS, axon initial segment; AP, action potential; GC, granule cell; DCN, deep cerebellar nuclei; FHF, fibroblast growth factor homologous factor; J, current density; KO, knockout; MF, mossy fiber; Na_V, Na^+ channel; PBS, phosphate buffered saline; PC, Purkinje cell; PF, parallel fiber; PKD, paroxysmal kinesigenic dyskinesia; PRRT2, PRoline-Rich Transmembrane protein-2; SD, somato-dendritic component; TTX, tetrodotoxin; WT, wild type.

* Corresponding author at: Center for Synaptic Neuroscience and Technology, Istituto Italiano di Tecnologia, Largo Rosanna Benzi 10, 16132 Genova, Italy.
E-mail address: fabio.benfenati@iit.it (F. Benfenati).

[1] Equal contribution.

[2] *Present address:* Department for BioMedical Research, Universität Bern, Bern, Switzerland.

https://doi.org/10.1016/j.nbd.2021.105275
Received 3 December 2020; Received in revised form 24 January 2021; Accepted 24 January 2021
Available online 28 January 2021

synapses that translates into hyperactivity and instability of neuronal networks (Valente et al., 2016a; Fruscione et al., 2018; Valente et al., 2019). In addition to its synaptic activity, we recently demonstrated that PRRT2 interacts with voltage-gated Na^+ channels $Na_V1.2/1.6$ - the two main voltage-gated Na^+ channel expressed in excitatory neurons - and negatively modulates their membrane expression (Fruscione et al., 2018; Lerche, 2018; Valente et al., 2019).

Consistent with the loss-of-function mechanism of the most frequent human PRRT2 mutations, PRRT2 knockout (KO) murine models well recapitulate the pathological hallmarks of PRRT2-associated paroxysmal disorders (Michetti et al., 2017a; Tan et al., 2018; Mo et al., 2019; Calame et al., 2020). We have initially shown that a constitutive PRRT2 KO mouse displays a paroxysmal motor phenotype characterized by loss of balance, bouncing behavior, dyskinetic movements, backward locomotion ("*moonwalking*") and repetitive grooming. The motor phenotype starts early in the postnatal life and persists in the adulthood. In addition, PRRT2 KO mice display an increased seizure propensity with sound-induced wild and explosive running episodes (Michetti et al., 2017a). Interestingly, the morphological analysis of heterozygous PRRT2 KO mice expressing β-galactosidase under the control of the PRRT2 promoter revealed PRRT2 expression in discrete brain regions, with the highest expression in cerebellar granule cells (GCs) (Michetti et al., 2017a). Consistently, specific deletion of PRRT2 in cerebellar GCs recapitulates the behavioral phenotype of PRRT2 KO mice (Tan et al., 2018). An implication of cerebellar GCs in PRRT2 pathology is also suggested by the marked and long-lasting facilitation of synaptic responses in PRRT2 KO parallel fiber (PF) to Purkinje cell (PC) synapses that was proportional to the stimulation frequency and triggered abnormal PC firing in response to GC optogenetic stimulation (Michetti et al., 2017a; Tan et al., 2018).

The cerebellum is central to motor control perfecting on-going adjustments of movement execution (D'Angelo and Casali, 2013). Together with the basal ganglia, the cerebellum participates in the expression of dystonic movements (Neychev et al., 2008; Chen et al., 2014; Fremont et al., 2014; Kross and De Zeeuw, 2018; Cook et al., 2020). The high expression of PRRT2 in GCs strongly supports a cerebellar role in the onset of paroxysmal attacks characterizing PKD (Michetti et al., 2017a). In agreement, mice in which PRRT2 was specifically removed from GCs became more prone to dystonic attacks (Tan et al., 2018). GCs represent the input stage of the cerebellum receiving sensory, proprioceptive, vestibular and motor information via mossy fibers (MFs) originating from several pre-cerebellar nuclei in the brainstem and spinal cord. These neurons show regular high frequency discharge upon pronounced long depolarization while they display particular patterns of activity and action potential (AP) organization at firing threshold (D'Angelo et al., 1998; D'Angelo et al., 2001). Together with transient Na^+ currents, persistent and resurgent Na^+ currents have been described in GCs (Magistretti et al., 2006; Afshari et al., 2004) and proposed to participate in AP clustering in response to limited depolarization (D'Angelo et al., 2001). During cerebellar development, GCs initially express $Na_V1.2$ channels that accumulate at the axon initial segment (AIS), while $Na_V1.6$ channels emerge at postnatal day 21 and their expression sharply increases thereafter. In adult mouse GCs, 90% of AISs are positive for both $Na_V1.6$ and $Na_V1.2$. Furthermore, $Na_V1.6$ is also expressed in GC dendrites (Osorio et al., 2010). Given the PRRT2-mediated negative modulation of membrane expression and biophysical properties of $Na_V1.2/1.6$ (Fruscione et al., 2018), the absence of functional PRRT2 could affect GC activity, not only acting at the level of GC-PC synapses (Michetti et al., 2017a; Tan et al., 2018), but also triggering GC hyperexcitability that will ultimately alter the cerebellar input at the MF-GC synapses.

In this paper, we have investigated the effects of PRRT2 deletion on the intrinsic excitability of GCs and the input-output relationships at the MF-GC synapses using primary granule cultures and acute cerebellar slices from constitutive PRRT2 KO mice. We show that primary mutant GCs display increased expression of Na^+ channels, increased amplitudes of transient Na^+ currents and increased length of the AIS, leading to an overall increase in intrinsic excitability. These results were fully confirmed in PRRT2 KO cerebellar slices, in which GCs were more prone to AP discharge in response to MF activation and displayed an enhancement of transient and persistent Na^+ currents, in the absence of changes at the mossy fiber-GC synapses. The results support a key role of GC PRRT2 in the physiological regulation of the excitatory input to the cerebellum and are consistent with a major role of a cerebellar dysfunction in the pathogenesis of PRRT2-linked paroxysmal pathologies.

2. Materials and methods

2.1. Breeding and genotyping of PRRT2 KO mice

PRRT2 KO mice were generated by EUCOMM/KOMP using a targeting strategy based on the 'knockout-first' allele (Skarnes et al., 2011; Michetti et al., 2017a). Mutant animals in a C57BL/6 N background were propagated as heterozygous colonies in the IIT SPF facility. Genotyping was performed by PCR with primers Prrt2_F: AGGTAGACGGGCATTTGAGC, Prrt2_R: CGTGGGGAAGAGGAGACAAC; CAS_R1_Term: TCGTGGTATC GTTATGCGCC, that were used to detect the wild type (WT) (Prrt2_F plus Prrt2_R product, 480 bp) and mutant (Prrt2_F plus Cas_R1_Term product, 200 bp) PRRT2 alleles and to genotype WT, heterozygous, and homozygous mice. The primer Prrt2_F, common to WT and mutant PCR, was designed in the intronic sequence between Prrt2 Exon 1 and Exon 2. The primers Prrt2_R and Cas_R1_Term were designed in the exon 2 of the PRRT2 gene and in the targeting cassette, respectively. All experiments were carried out in accordance with the guidelines established by the European Communities Council (Directive 2010/63/EU of 4 March 2014) and were approved by the Italian Ministry of Health (authorization n. 73/2014-PR and n. 1276/2015-PR).

2.2. Primary cultures of cerebellar granule cells

Primary cultures of low-density GCs neurons were prepared from WT and PRRT2 KO mice as described in Lee et al. (2009), with some modifications. Briefly, 7-day-old mice were sacrificed by CO_2 inhalation and cerebella were dissected out and collected in phosphate buffered saline (PBS). Then, the minced tissue was added to a dissociation system kit for cell culture preparation (Worthington Biochemical Corporation, Lakewood, NJ) and the mixture was equilibrated in a 5% CO_2 incubator at 37 °C. Tissue was dissociated by incubation with activated papain at 37 °C for 15–20 min, followed by mechanical trituration. Dissociated cells were pelleted and then resuspended in medium containing ovomucoid, a papain inhibitor. Intact cells were separated from broken cells by centrifugation through a single step discontinuous density gradient. The pellet was finally re-suspended in Neurobasal A + 1% Penicillin-Streptomycin +1% Glutamax +250 μM KCl + B27 and plated at different concentration for the experiments. No antimitotic drugs were added to prevent glia proliferation. Primary cultures of GCs were incubated at 37 °C in 5% CO_2 and half of the culture medium was changed every 4 days.

2.3. Immunoblot analysis

For western blotting analysis, protein concentration of the samples was determined using the BCA assay and equivalent amounts of protein were subjected to SDS-PAGE on polyacrylamide gels and blotted onto nitrocellulose membranes (Whatman, ThermoFisher Scientific, Waltham, MA). Blotted membranes were blocked for 1 h in 5% milk in Tris-buffered saline (10 mM Tris, 150 mM NaCl, pH 8.0) plus 0.1% Triton X-100 and incubated overnight at 4 °C with pan-Na_V (1:300, Sigma Aldrich, St. Louis, MO), PRRT2 (1:1000, Sigma Aldrich, St. Louis, MO) and actin (1:1000, Sigma Aldrich, St. Louis, MO) specific antibodies.

After washing, membranes were incubated for 1 h at room temperature with peroxidase-conjugated secondary antibodies and immunoreactive protein bands were revealed with the ECL chemiluminescence detection system (ThermoFisher Scientific) and quantified by densitometric analysis.

2.4. Immunocytochemistry of the axon initial segment

Immunofluorescence of the axon initial segment (AIS) in primary GCs was performed as previously described (Fruscione et al., 2018; Prestigio et al., 2019). Cells were fixed at 10 days in vitro (DIV) and probed with pan-Na_V (1:100, Sigma Aldrich, St. Louis, MO) and AnkyrinG (1:200, Santa Cruz Biotechnology, Inc., TX). To quantify the immunofluorescence intensity at the AIS, images were acquired with a Leica SP8 confocal microscope using a 63× oil-objective and 1024 × 1024 pixels (1 pixel = 0.24 μm) in z-stack with 0.3 μm steps. To analyze stack images, a Matlab script freely available at: www.mathworks.com/matlabcentral/fileexchange/28181-ais-quantification was used as previously described (Grubb and Burrone, 2010; Fruscione et al., 2018). Briefly, a line profile was drawn along the fluorescently labeled AIS from the soma through and 5 μm past the AIS. Pixel fluorescence intensity values were averaged over a 3 × 3 pixel square centered on an arbitrarily drawn line, which was then smoothened using a 40-point sliding mean and normalized between 1 and 0 (maximum and minimum fluorescence intensity). The maximum position of the AIS was determined at the peak of the smoothed and normalized profile of fluorescence intensity. The start and end positions of the AIS were the proximal and distal sites, respectively, at which the profile dropped to 33% of its peak.

2.5. Patch-clamp recordings in primary granule cells

Whole-cell patch-clamp recordings were conducted on primary culture of GCs plated at low-density (≈ 500 cells /mm^2) and kept 7–12 DIV. All recordings were performed using an EPC-10 amplifier (HEKA Electronik, Reutlingen, Germany) using patch pipettes prepared from thin-borosilicate glass (Hilgenberg GmbH, Malsfeld, Germany) and pulled to a final resistance of 2–3 MΩ when filled with standard internal solution. Voltage-gated Na^+ currents were recorded in whole-cell configuration using an internal solution containing (in mM): 100 CsCl, 30 CsF, 10 NaCl, 1 $MgCl_2$, 0.5 $CaCl_2$, 10 HEPES, 10 EGTA, 4 Mg-ATP and 0.4 Na-GTP, pH 7.3 with CsOH. The extracellular solution contained (in mM): 120 NaCl, 3 KCl, 2 $CaCl_2$, 1 $MgCl_2$, 11 glucose, 10 HEPES, 0.5 $CdCl_2$, 20 TEA-Cl and 1 4-aminopyridine, pH 7.3 with NaOH (Osorio et al., 2005). Data acquisition was performed using PatchMaster programs (HEKA Elektronik). Transient and leakage currents were digitally subtracted using the P/N leak subtraction procedure. Whole-cell family currents of fast inactivating voltage gated Na^+ channels were evoked by 5 mV steps depolarization from −85 to 70 mV with a holding potential of −90 mV. Steady-state of fast inactivation curves were studied by recording the peak currents amplitude evoked by 20-ms test pulses to −10 mV after 500-ms pre-pulses to potentials over the range of −130 to 10 mV. Time-dependent rate of recovery from fast inactivation was calculated by pre-pulsing the cell with a 20-ms step to −20 mV to inactivate the channels and then bringing back the potential to −100 mV for increasing recovery durations (0.5, 1, 2, 4, 8, 32, 64, 128, 148 ms) before the test pulse of −20 mV. The Na^+ current density (J) was obtained by dividing the peak inward current by the cell capacitance (nA/pF). The conductance/voltage relationship (G-V) curves were obtained by converting the maximal current values, evoked with the voltage step protocols, to conductance using the relation $G_{Na} = I_{Na} / (V\text{-}E_{Na})$, where G_{Na} is the Na^+ conductance, I_{Na} is the peak Na^+ current, V is the command pulse potential, and E_{Na} is the experimentally determined reversal potential of Na^+ current obtained from the J/V curves. The normalized activation and inactivation curves for each cell were fitted to the Boltzmann equation in the form: $Y = 1/\{1 + \exp.[(V—V_{0.5})/k]\}$, where Y is the normalized G_{Na} or I_{Na}, V is the command pulse potential, $V_{0.5}$ is the voltage required to activate the half-maximal conductance or inactivation, and k is the slope of curve in $V_{0.5}$.

Recordings of GC firing properties were performed using the current-clamp configuration using a standard internal solution containing (in mM): 126 K^+ gluconate, 4 NaCl, 1 $MgSO_4$, 0.02 $CaCl_2$, 0.1 BAPTA, 15 glucose, 5 HEPES, 3 ATP, 0.1 GTP, pH 7.2 with KOH. Cells were maintained in a standard external solution containing (in mM): 140 NaCl, 2 $CaCl_2$, 1 $MgCl_2$, 4 KCl, 10 glucose, 10 HEPES, pH 7.3 with NaOH. In all recordings, D-AP5 (50 μM), CNQX (10 μM), CGP (10 μM) and BIC (30 μM) were added to the external solution to block NMDA, non-NMDA, $GABA_A$ and $GABA_B$ receptors, respectively. The rheobase was calculated as the minimum depolarizing current needed to elicit at least one AP. Input resistance was calculated using the Ohm law in the linear region of the voltage-current relationship determined after injecting hyperpolarizing/depolarizing current steps (−10, −5, 5, 10 pA) in neurons maintained at a holding potential of −70 mV. For each recorded cell, the plot of the time derivative of voltage (dV/dt) versus voltage (phase-plane plot) was determined from the first action potential elicited by the minimal current injection. This plot was used to extract threshold potential, maximum rising slope and peak potential (V_{max}). Amplitude of APs was calculated as the difference between the V_{max} and the threshold value. For the determination of evoked firing, GCs were current clamped at −70 mV and APs were elicited by 5 pA steps lasting 1000 ms applied every 2 s. The instantaneous and mean firing frequencies were determined at the minimal value of injected current able to evoke two or more APs. The instantaneous firing frequency was estimated as the reciprocal value of the time difference between the first two evoked APs. The mean firing frequency was calculated as the ratio of the number of APs to the time interval between the first and the last evoked action potential (Valente et al., 2016b). The threshold and rheobase ramps were calculated on the firing properties of GCs stimulated by a slow ramp (10 s) of current injection (increments of 10 pA) with cell held at −70 mV after a first step of 30 pA to approach membrane threshold. Series resistance was compensated 80% (2-μs response time) and the compensation was readjusted before each stimulus. The shown potentials were not corrected for the measured liquid junction potential of 9 mV. Recordings with either leak currents >100 pA or series resistance >20 MΩ were discarded. All recordings were performed at 22–24 °C. Voltage-clamp recordings of voltage-gated Na^+ current and current-clamp recordings were acquired at 20 kHz and low-pass filtered at 4 kHz, while the action potential shape was studied with a sampling frequency of 50 kHz, lowpass filtered at 10 kHz.

2.6. Electrophysiology in acute cerebellar slices

Acute cerebellar slices were prepared from PRRT2 KO mice, WT littermates or C57Bl6/N age-matched animals. Adult (at least 7 weeks old mice) female and male mice were used for the recordings. Briefly, mice were anesthetized with a short isoflurane exposure, decapitated and the cerebellum quickly dissected in ice-cold 95% O_2 / 5% CO_2 bubbled Krebs buffer containing (in mM): NaCl 120, KH_2PO_4 1.18, KCl 2, $MgSO_4$ 1.2, $CaCl_2$ 2, $NaHCO_3$ 26 and glucose 24 mM. Sagittal 300-μm slices were cut with a vibratome and let recover at least 30 min in bubbled Krebs buffer at room temperature before starting the experiments. Electrophysiological experiments were performed with a MultiClamp 700B amplifier and data acquired via the Clampex software (Molecular Devices, San Jose, CA). Patch-clamp experiments in whole-cell configuration were performed at room temperature in 95% O_2/5% CO_2 bubbled Krebs buffer supplemented with SR95531 and strychnine (5 and 1 μM, respectively; Tocris Bioscience, Bristol, UK) to block GABAergic and glycinergic inhibitory transmission respectively. Thick wall patch pipettes with a 7–8 ΩM final resistance were pulled with a horizontal puller (Sutter Instruments, Novato, CA) and filled with a K-gluconate-based intracellular solution containing (in mM): K-gluconate 126, NaCl 4, $CaCl_2$ 0.02, $MgSO_4$ 1, BAPTA 0.1, MgATP 3, NaGTP 0.1, HEPES 5 and glucose 15, pH 7.2.

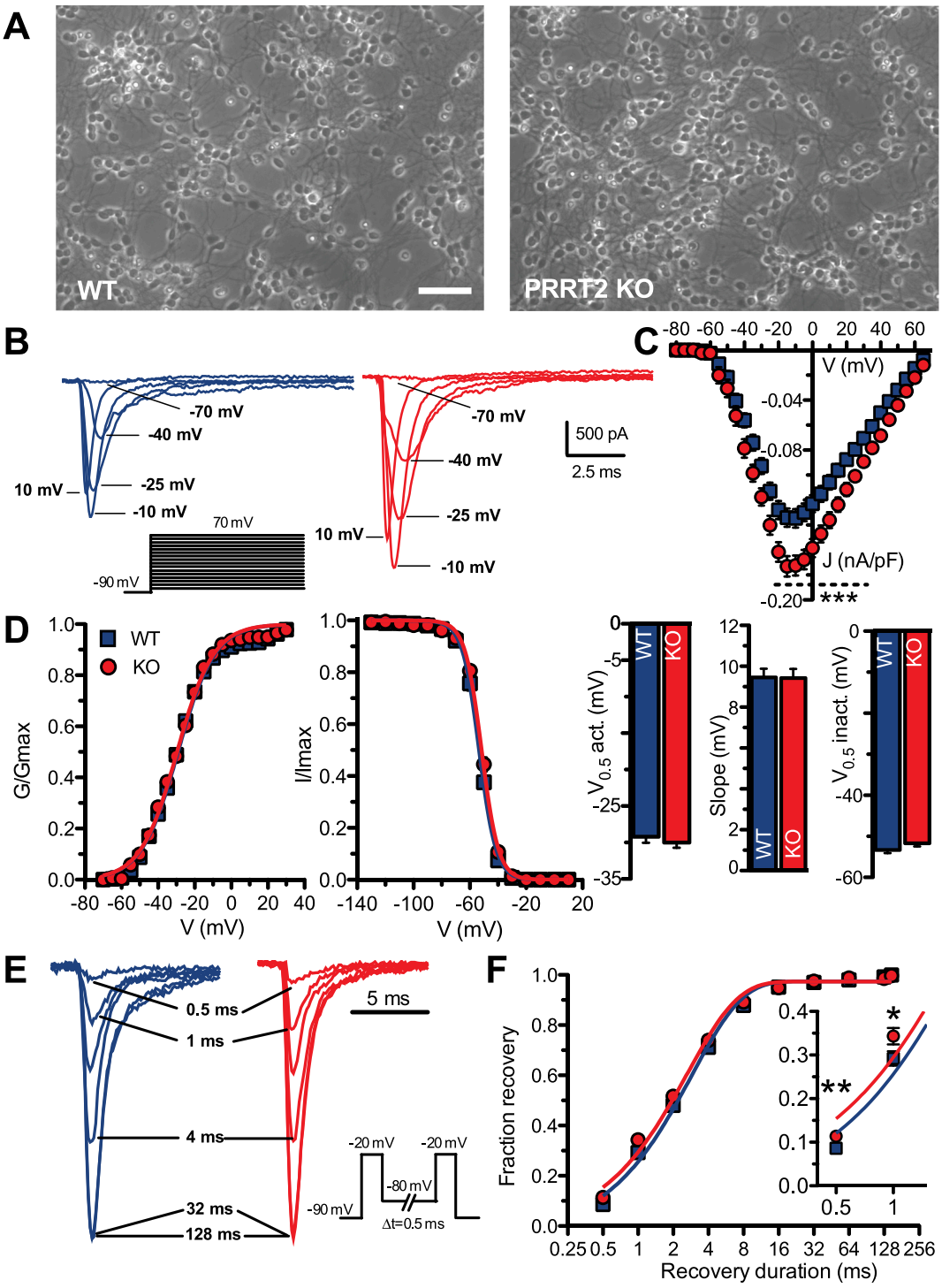

Fig. 1. Voltage-gated Na^+ channels are negatively regulated by PRRT2 in primary cultures of cerebellar granule cells.
A. Phase-contrast micrographs of typical networks formed by primary GCs (7 DIV) prepared from WT (*left*) and PRRT2 KO (*right*) mice. Scale bar, 200 µm. B. Representative whole-cell Na^+ currents recorded in WT (*left*, blue) and PRRT2 KO (*right*, red) GCs elicited by a protocol (inset) consisting of 5-mV depolarization steps from −80 to 70 mV from a holding potential of −90 mV. For clarity, four representative current traces per genotype are plotted. C. Current density (J) versus voltage relationship for WT and PRRT2 KO GCs. Data are means ± sem (WT, $n = 52$; PRRT2 KO, $n = 47$). D. Voltage-dependence of conductance (G/G_{max}) and steady-state inactivation curves for both genotypes. The lines are the best-fitted Boltzmann curves and the activation half-maximal voltages ($V_{0.5\ act.}$), slope of activation curve and inactivation half-maximal voltages ($V_{0.5\ inact.}$) are plotted on the right. Data are means ± sem (WT, n = 52; PRRT2 KO, n = 47). E. Family of representative whole-cell current traces normalized to the peak from WT and PRRT2 KO GCs showing the rate of recovery from fast inactivation at −80 mV. In the protocol (inset), neurons were first pulsed to −20 mV from a holding potential of −90 mV, brought back to the recovery potential (−80 mV) for increasing recovery periods (0.5 to 130 ms) before the second test pulse to −20 mV. The time indicated in the traces corresponds to the duration of the recovery period. F. Time-dependent rate of recovery from fast inactivation for the two genotypes studied as in E, shown in a semilogarithmic scale. The time scale of the first two points is expanded in the inset for clarity. Data are means ± sem (WT, $n = 42$; PRRT2 KO, $n = 40$). *$p < 0.05$, **$p < 0.01$, ***$p < 0.001$ unpaired Student's *t*-test/Mann-Whitney's *U* test.

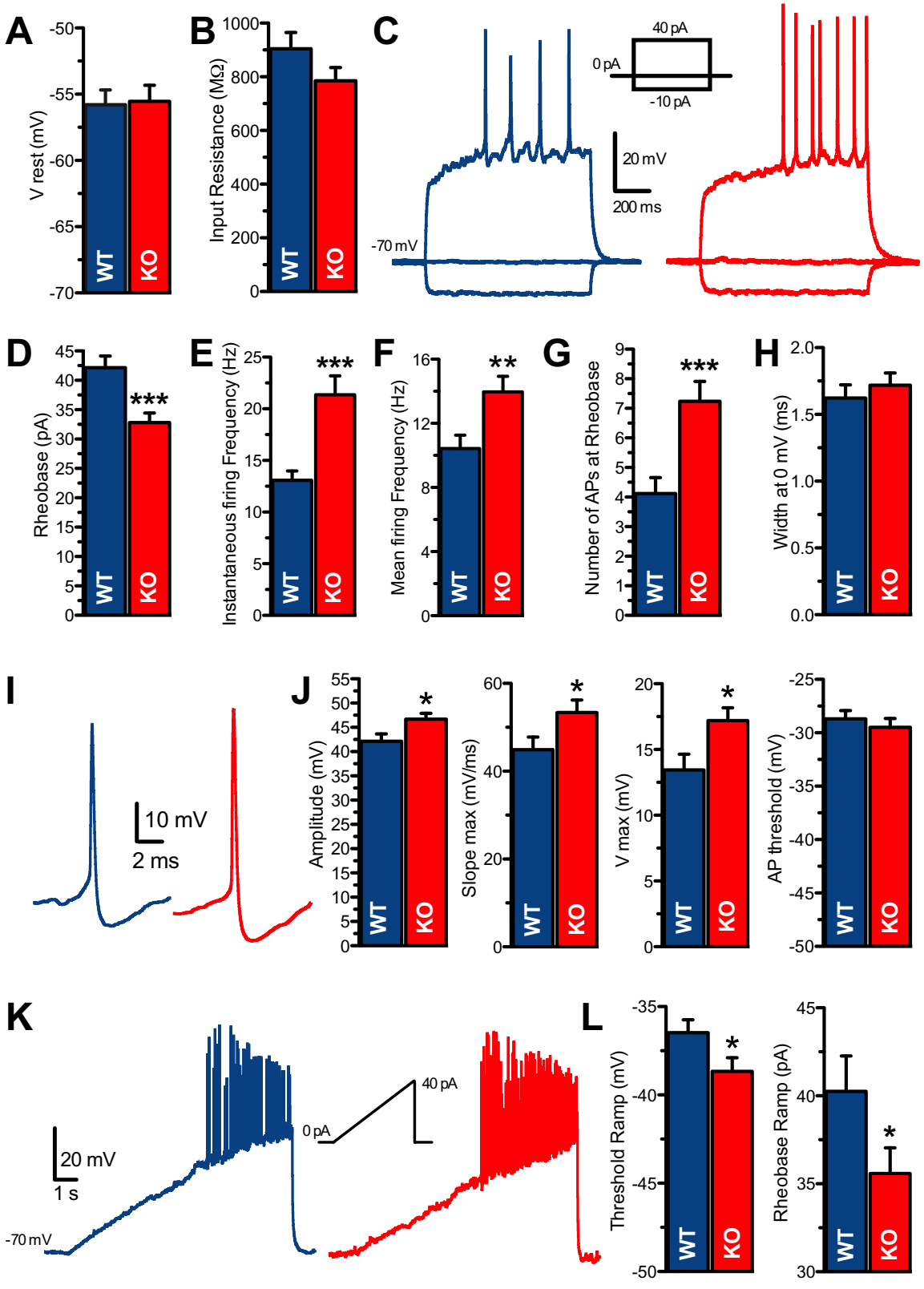

(caption on next page)

Fig. 2. PRRT2 KO granule cell neurons display an increased intrinsic excitability.
A,B. Mean (± sem) resting membrane potential and input resistance recorded in WT (blue) and PRRT2 KO (red) low-density primary GCs (WT, $n = 35$ and 60; PRRT2 KO, $n = 33$ and 59; for panels A and B, respectively). C. Representative current-clamp recordings of action potentials evoked in WT and PRRT2 KO GCs by 1-s current step at 40 pA. D—H. Mean (± sem) values of rheobase (WT, $n = 60$; KO, $n = 59$), instantaneous firing frequency (WT, $n = 57$; KO, n = 59), mean firing frequency (WT, n = 57; KO, n = 59), AP number at rheobase (WT, n = 60; KO, n = 59) and action potential width measured at 0 mV (WT, $n = 54$; KO, n = 57), for both genotypes. I. Representative shapes of the first evoked AP recorded in WT (blue) and PRRT2 KO (red) GCs. J. *From left to right*: amplitude, maximal slope, maximal voltage and AP threshold calculated for the first AP evoked by minimal current injection in GCs of both genotypes (WT, n = 60; KO, n = 59). K. Representative current-clamp recordings of APs evoked by 40 pA current injection over a 10-s slow ramp (inset) for WT (blue) and PRRT2 KO (red) GCs. L. Mean (± sem) threshold and rheobase values calculated in GCs from both genotypes subjected to the ramp protocol showed in K (WT, n = 40; KO, $n = 43$). *$p < 0.05$, **p < 0.01, ***p < 0.001; unpaired Student's *t*-test/Mann-Whitney's *U* test.

GCs in the anterior cerebellum were targeted, with most of the recorded cells located in lobule VI, that receives MF from pontine nuclei that are mostly negative for PRRT2 (Michetti et al., 2017a). Typical all-or-none MF-mediated excitatory post-synaptic currents (EPSCs; Silver et al., 1996) were induced by white-matter electrical stimulation via a glass pipette filled with extracellular recoding solution. The stimulation strength was progressively raised and set to the minimum value required to induce MF-evoked EPSCs in GCs voltage-clamped at −70 mV. Currents were lowpass filtered at 1 KHz and digitized at 5 KHz. Following EPSC recordings, cells were switched to current-clamp mode, held at −70 mV and GCs firing properties were investigated by applying 1-s depolarizing steps of 2.5 pA. AP characteristics were measured on the first AP elicited by the applied protocol. MF-mediated membrane voltage depolarization was induced by applying 5 or 20 consecutive stimuli at 10, 20, 50, 100, 200 and 400 Hz. Traces were filtered at 10 KHz and digitized at 50 KHz. To stimulate single MFs, the stimulation intensity was set to the minimal level required to obtain the typical all-or-none MF-mediated response in the recorded GC. Increasing the stimulation strength beyond this point elicited EPSCs of larger amplitude and separated in discrete steps. Since GCs are innervated by 3 to 5 MFs, with each MF forming a single synapse, each activation level reflects the progressive recruitment of additional MFs, with EPSC elicited at minimal stimulation originating from a single input (Sola et al., 2004).

Whole-cell Na^+ currents were recorded under experimental conditions favoring their isolation; the extracellular recording solution contained (in mM): NaCl 100, TEA-Cl 19.25. KCl 3, $MgCl_2$, 2 $CaCl_2$ 2, $BaCl_2$ 2, $CdCl_2$ 0.5, 4-AP 0.1, $NaHCO_3$ 26 and glucose 11. Patch pipettes were filled with following intracellular solution (mM): CsF 104, TEA-Cl 50, $MgCl_2$ 2, HEPES 10, EGTA 10, NaATP 2, NaGTP 0.2, pH 7.2 (Osorio et al., 2010). Tetrodotoxin (TTX) 1 μM was added at the end of each recording session and Na^+ currents routinely isolated by subtracting the TTX-insensitive trace from the control trace. GCs were voltage-clamped at −80 mV and transient currents were elicited by progressively depolarizing the membrane voltage from −75 mV to 15 mV with 5-mV steps lasting 20 ms. Inactivation was investigated with a test step of 50 ms at −10 mV proceeded by 125-ms long conditioning step changing the membrane voltage from −85 mV to −15 mV in 5-mV increments. Persistent currents were recorded by applying 500 ms-long depolarizing steps from −75 mV to −15 mV with 5 mV increments and quantified at the end of the depolarizing step where transient currents were inactivated. Resurgent currents were recorded by depolarizing the membrane voltage from −40 mV to −15 mV with a 100 ms-long step and 5 mV increment after an inactivating pre-pulse of 20 ms at 0 mV.

Whole-cell recordings were analyzed with Clampfit. The AP threshold was quantified with the phase plot analysis and calculated as the membrane voltage value at which the AP first derivative is equal to 10. AP height was defined as the AP amplitude in relation to the after hyperpolarization and AP width was measured at 50% of the AP amplitude. Just-threshold (defined as the first depolarizing step inducing more than 2 APs) burst analysis was performed in Clampfit using the mean inter-event interval detection method with a minimum of 2 APs/burst. At each current step, AP bursts were separated when the interval between consecutive APs was greater than the mean interspike interval.

2.7. Statistical analysis

Data are expressed as means ± sem for number of cells (n) or mouse preparations as described in the figure legends. Normal distribution of data was assessed using the D'Agostino-Pearson's normality test. The F test was used to compare variance between two sample groups. To compare two sample groups, either the two-tailed Student's *t*-test or the Mann-Whitney *U* test was used depending on whether data were normally or non-normally distributed. To compare more than two normally distributed sample groups, one-way or two-way ANOVA followed by the Fisher exact test was used. Alpha levels for all tests were 0.05%. Statistical analysis was performed using OriginPro-8 (OriginLab Corporation, Northampton, MA) and Prism (GraphPad Software, San Diego, CA) softwares.

3. Results

3.1. Increase of transient voltage-gated Na^+ currents in cultured PRRT2 KO granule cells

To examine the functional consequences of PRRT2 loss on voltage-gated Na^+ currents, we performed electrophysiological recordings in low-density cultures of primary GCs (7–12 DIV) obtained from 7-days-old WT and PRRT2 KO mice (Fig. 1A). Whole-cell current recordings by voltage-step depolarization ($V_h = -90$ mV) showed that, in the absence of PRRT2, the amplitude of fast activating-inactivating Na^+ currents were significantly enhanced (Fig. 1B). However, the density (J = nA/pF) versus voltage relationships showed that Na^+ currents had the same kinetic properties in both genotypes (Fig. 1C). The voltage-dependence of activation and inactivation as a function of the membrane voltage were measured by fitting the G/G_{max} and I/I_{max} curves with the Boltzmann equation. The membrane potential at half-maximal activation ($V_{0.5}$) and inactivation, as well as the slope of activation were not affected by loss of PRRT2 suggesting that the absence of PRRT2 does not affect the voltage-dependent properties of Na^+ channels in primary cerebellar GCs (Fig. 1D). The kinetics of recovery from fast inactivation was also similar in both genotypes (Fig. 1E,F), although a significant increase of the Na^+ channel recovery fraction was observed at the shortest interpulse intervals in PRRT2 KO GCs (Fig. 1F, inset). These results indicate that the absence of PRRT2 expression in GCs is associated with an enhancement of the Na^+ current density, in the absence of substantial changes in the biophysical properties of the channels.

3.2. PRRT2 deletion increases the intrinsic excitability of primary cerebellar granule cells

The observed effects of PRRT2 deficiency on voltage-gated Na^+ currents led us to investigate GC intrinsic excitability. Patch-clamp recordings in current-clamp configuration revealed that, while WT and PRRT2 KO GCs exhibited similar resting membrane potentials and input resistances (Fig. 2A,B), they showed different intrinsic properties (Fig. 2C). Indeed, PRRT2 KO GCs were characterized by a significant decrease in the rheobase paired by an increase in instantaneous and mean firing frequencies and in the number of APs evoked at the rheobase, while the width at 0 mV of the first evoked AP remained

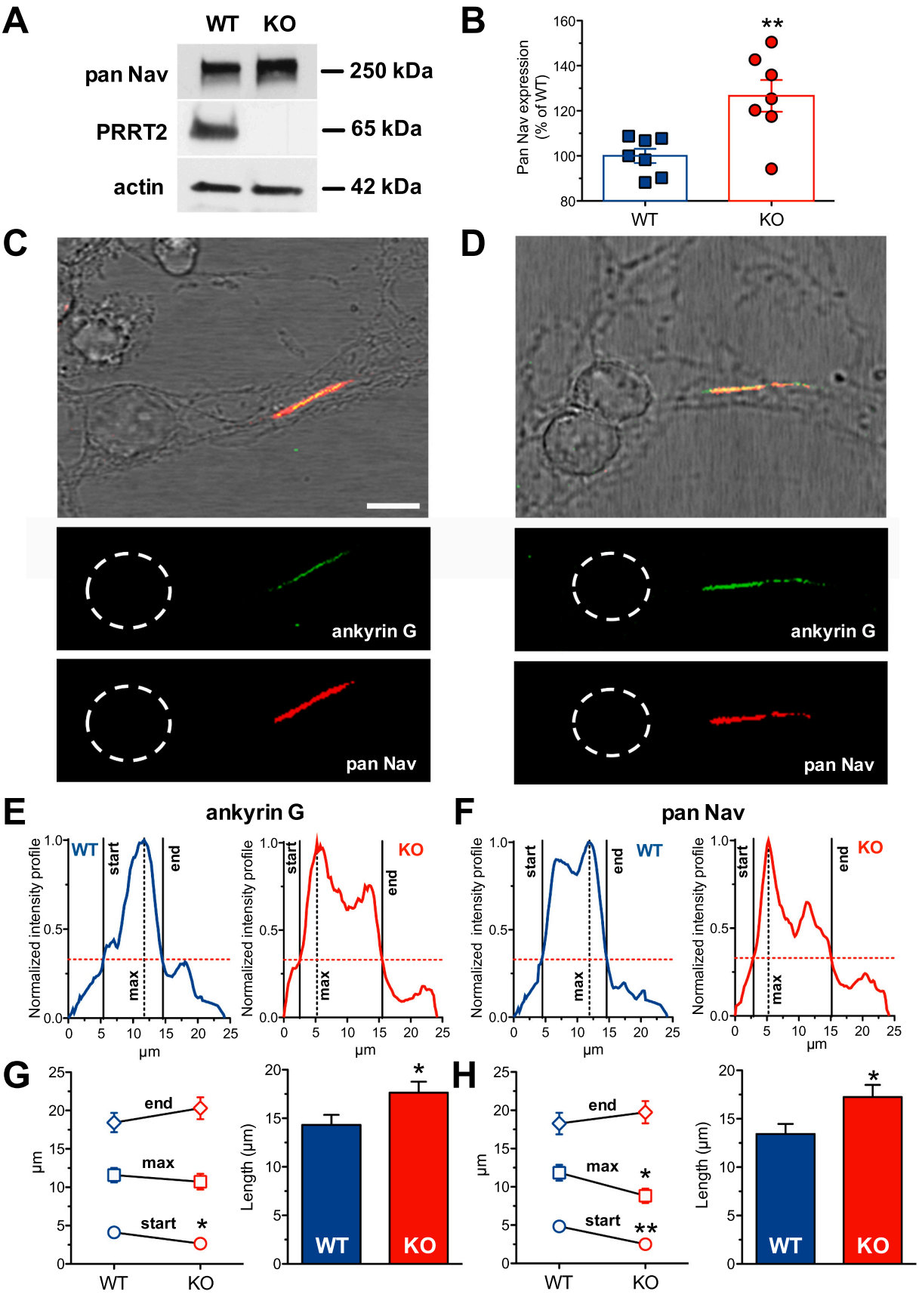

(caption on next page)

Fig. 3. PRRT2 deletion increases the expression of Na^+ channels and the length of the axon initial segment in primary granule cells.
A. Representative immunoblots of pan-Na_V and PRRT2 immunoreactivities in primary GC lysates from WT and PRRT2 KO mice. Actin immunoreactivity was included as control of equal loading. B. Quantification of Na_V channel expression in WT and PRRT2 KO mice normalized on actin immunoreactivity and expressed in percent of the mean WT immunoreactivity (mean ± sem with superimposed individual values; $n = 7$ from 3 independent preparations per genotype). C,D. Representative images of WT (C) and PRRT2 KO (D) primary GCs (10 DIV) immunostained for AnkyrinG (green) and pan-Na_V (red). The upper panels are the merged phase contrast and double fluorescence images. Cell bodies are circled in the fluorescence images. Scale bar, 2 μm. E,F. Representative fluorescence intensity profiles of AnkyrinG (E) and pan-Na_V (F) signals along the axon of WT (blue) and PRRT2 KO (red) GCs used to measure the AIS start, end and maximum. The horizontal red line represents the threshold fluorescence used to define AIS limits. G. Distance of AIS start, maximum and end from the cell body in WT (blue symbols) and PRRT2 KO (red symbols) neurons based on the distribution of AnkyrinG (*left*) and pan-Na_V (*right*) immunoreactivities. H. Mean (± sem) AIS length measured in AnkyrinG (*left*) and pan-Na_V (*right*) labeled GCs from WT (blue) and PRRT2 KO (red) mice ($n = 25$ GCs for both conditions from n = 3 independent cell preparations). *$p < 0.05$; **$p < 0.01$; Mann-Whitney *U* test.

unchanged (Fig. 2D-H). When we studied in more detail the waveform of the first AP evoked at the rheobase (Fig. 2I), PRRT2 KO GCs exhibited an increase in AP amplitude, slope of the rising phase and maximal peak potential (V_{max}), in the absence of effect on the threshold potential (Fig. 2J). Because the lack of effect on AP threshold could be due to the coarse stimulation of cell firing (injection of 5 pA steps), we used a more accurate protocol for firing activation by injecting a 10-s slow ramp current (Fig. 2K). Using ramp stimulations, we observed that PRRT2 KO GCs had a significantly more negative threshold for AP activation paired by a decreased rheobase (Fig. 2L). Collectively, these data testify that primary cerebellar GCs lacking PRRT2 are hyperexcitable and display alterations of AP waveforms that are compatible with the increased Na^+ currents.

3.3. PRRT2 deletion increases the expression of Na^+ channels and the length of the axon initial segment in cerebellar granule cells

The electrophysiological phenotype of primary PRRT2 KO GCs and the reported interaction between PRRT2 and Na_V channels (Fruscione et al., 2018) brought us to investigate whether PRRT2 deletion affects the Na^+ channel expression and localization at the AIS in primary GCs. We first evaluated the overall expression of Na^+ channels in extracts of primary GCs from WT and PRRT2 KO mice using a pan-Na_V specific antibody. Consistent with the electrophysiological data, PRRT2 KO GCs expressed higher levels of Na^+ channels than WT GCs (Fig. 3A,B). To investigate the molecular basis for the increased intrinsic excitability of PRRT2 KO GCs, we investigated the distribution of Na^+ channels in the AIS, the domain responsible for the initiation of the AP (Fig. 3C,D). WT and PRRT2 KO GC cultures were double immunostained with AnkyrinG and pan-Na_V antibodies and the intensity profiles of both markers were analyzed as a function of the distance from the cell body (Fig. 3E,F; see Materials and Methods). The length of the AIS, evaluated from the intensity profiles of both AnkyrinG (Fig. 3G) and pan-Na_V (Fig. 3H). immunoreactivites, was significantly increased in PRRT2 KO GCs as compared to WT GCs. Interestingly, the increase in length was entirely attributable to the AIS start that was significantly closer to the cell body in PRRT2 KO GCs than in WT GCs (Fig. 3G,H; left panels). This demonstrates that the increased intrinsic excitability of primary mutant GCs is paralleled by a longer AIS that originates closer to the cell body.

3.4. Lack of PRRT2 facilitates mossy fiber-induced granule cell firing in cerebellar slices

The effects of PRRT2 deficiency on the intrinsic excitability of GCs in primary cultures led us to investigate the same cells in a more physiological environment. Thus, we evaluated the impact of PRRT2 ablation on GC synaptic integration of MF input in PRRT2 KO and WT acute cerebellar slices by whole-cell patch-clamp recordings of GCs paired with MF electrical stimulation. Because of the expression of PRRT2 in some pre-cerebellar nuclei (Michetti et al., 2017a) and the reported effects of PRRT2 deficiency on fast synchronous release (Valente et al., 2016a), we first analyzed MF-induced EPSCs and short-term plasticity in GCs to exclude any functional change at these synaptic inputs in the absence of PRRT2. Stimulation of a single MF (see Materials and Methods) elicited EPSCs in GCs of similar amplitude in WT and PRRT2 KO slices (Fig. 4A). Charge and kinetics of EPSCs were also unaltered in PRRT2 KO GCs (not shown). Moreover, the paired-pulse depression characterizing MF-GC synapses at shorter interpulse intervals (Xu-Friedman and Regehr, 2003) was unaltered in PRRT2 KO compared to WT slices (Fig. 4B). These data support the notion that synaptic transmission at MF-GCs synapses is not affected by the PRRT2 deletion under our experimental conditions.

We next investigated the GC synaptic integration properties in response to single MF activation by applying 5 (Fig. 4C,D) or 20 (Fig. 4E, F) pulses at increasing frequencies (from 10 to 400 Hz). The cumulative distribution of APs elicited at various input frequencies revealed the presence of an increased excitability of GCs in PRRT2 KO cerebellar slices. Five consecutive stimulations were poorly effective in inducing GC firing in WT slices, with 81–96% of WT cells remaining silent at all tested frequencies (Fig. 4C). On the contrary, raising the stimulation frequency progressively increased the percentage of firing cells in PRRT2 KO slices from 12% at 10 Hz to 59% at 400 Hz (Fig. 4D). This increment was more pronounced in response to 20 stimuli, with virtually all PRRT2 KO GCs firing at an input frequency of 400 Hz (Fig. 4F, *yellow triangle*), whereas only 45% of WT GCs reached the firing threshold under the same conditions (Fig. 4E, *yellow triangle*). Statistical analysis revealed a highly significant increase in the number of firing PRRT2 KO GCs at 200 Hz (5 stimuli), 400 Hz (5 and 20 stimuli) and at 100 Hz (20 stimuli) (Fig. 4G,H).

3.5. PRRT2 KO granule cells display multiple action potential discharge profiles in acute cerebellar slices

Granule cells receive typical physiological inputs at 50–100 Hz (Rancz et al., 2007) and can discharge multiple, clustered APs upon just-threshold depolarization. When GCs were stimulated by trains of 20 stimuli administered at increasing frequencies, mostly silent WT GCs responded with few single APs, while PRRT2-KO GCs displayed a clear propensity to fire double APs already at low frequency of stimulation (10 Hz; Fig. 5A; Suppl. Fig. 1). Multiple APs (> 2 APs) were effectively induced with a 50 Hz train in PRRT2-KO, while WT neurons required higher stimulation frequencies to be brought to firing, with multiple APs appearing only after the last stimulus of >100 Hz trains (Suppl. Fig. 1). We therefore quantified the percentage of the total applied stimuli that induced two or more APs immediately after each single stimulation for each input frequency in WT and PRRT2 KO slices. Increasing the frequency of MF stimulation progressively enhanced the probability of GC repetitive firing/stimulus with peak values at 50 and > 100 Hz in PRRT2 KO and WT slices, respectively (Fig. 5B). Up to 100 Hz input frequency, the percentage of stimuli able to trigger multiple APs was larger in PRRT2 KO compared to WT slices, with a significant difference at 50 Hz (Fig. 5B, *inset*). We also measured the firing frequency of the multiple APs elicited per single stimulus (intra-stimulus frequency). Since no correlation was detected between the input frequency and the intra-stimulus frequency in both WT and PRRT2 KO slices (Fig. 5C), data were pooled and the intra-stimulus frequency quantified. When compared to the WT, PRRT2 KO GCs displayed a highly significant increase in the overall intra-stimulus frequency (Fig. 5D).

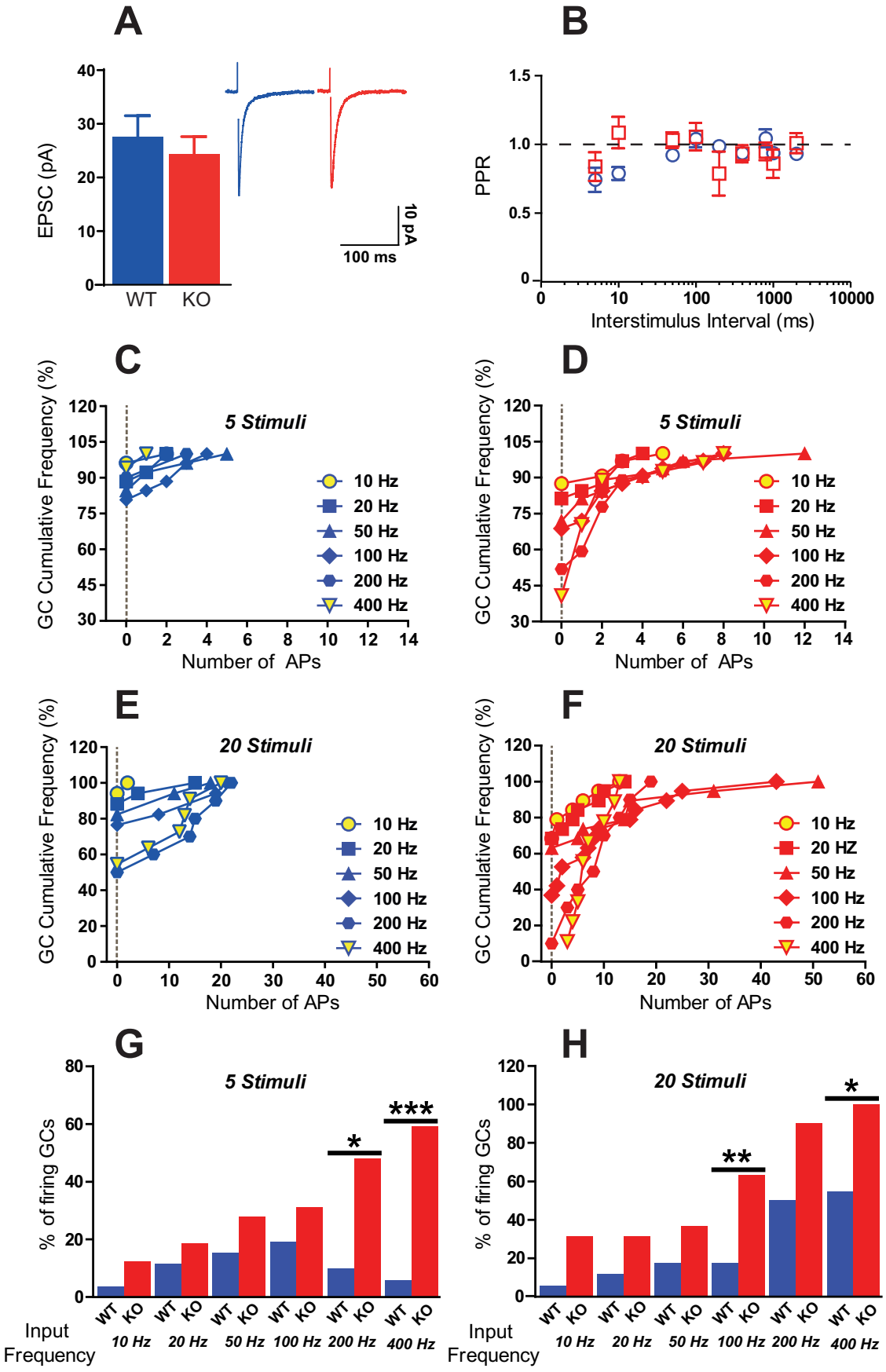

(caption on next page)

Fig. 4. Increased firing propensity of PRRT2 KO granule cells in acute cerebellar slices.
A,B. Representative currents (inset; stimulation artifacts were blanked for clarity) and amplitude of MF to GC synaptic currents (A) and paired-pulse ratio (PPR; $EPSC_1/EPSC_2$; B) studied in WT (blue) and PRRT2 KO (red) GCs show no significant difference between the two genotypes (WT, n = 25; KO, *n* = 39). C—F. WT (C,E) and PRRT2 KO (D,F) GC firing in response to MF repeated stimulation with either 5 (C,D) or 20 (E,F) stimuli at increasing frequencies (10–400 Hz). PRRT2 KO GCs reached the firing threshold more easily with respect to WT GCs, as shown by the reduced percentage of silent GCs (number of AP = 0) in the mutant compared to the WT slices at each input frequency tested. In both WT and PRRT2 KO GCs, yellow circles and yellow triangles represent the GC response to 10 and 400 Hz stimulation, respectively. G,H. Frequency distribution of GC firing in WT (blue) and PRRT2 KO (red) cerebellar slices as a function of the input frequency. The number of firing GCs in response to either 5 (G) or 20 (H) stimuli is expressed in percentage of the total number of GCs. The data reveal an increased percentage of responding GCs upon MF stimulation at each tested frequency in PRRT2 KO as compared to WT GCs. WT, 10–100 Hz, *n* = 26; 200 Hz, *n* = 20; 400 Hz, *n* = 17. PRRT2 KO, 10–100 Hz, *n* = 32; 200 Hz and 400 Hz, *n* = 27. *p < 0.05, **p < 0.01, ***$p < 0.001$; Fisher's exact test.

Just-threshold bursting behavior was further investigated by current-clamp experiments and highlighted significant differences between WT and PRRT2 KO GCs. As expected, 1-s membrane depolarization elicited bursts in both WT and PRRT2 KO GCs (Fig. 5E). However, the intra-burst frequency was significantly higher in PRRT2 KO GCs compared to WT GCs, although the number of APs/burst was comparable between the two genotypes (Fig. 5F), Taken together, these data support an increased responsiveness at the input stage of the cerebellum in PRRT2 KO mice. Mossy fiber activation was more effective in triggering GCs firing in the absence of PRRT2 and GCs' propensity to fire multiple APs was also increased. Moreover, multiple APs were discharged at higher frequency upon stimulation in the KO compared to the WT.

3.6. PRRT2 deletion modulates granule cell firing properties in cerebellar slices

The positive modulation of Na^+ channels expression occurring in the absence of PRRT2 supports an increase GC excitability as the underlying mechanism of the previously described enhanced responsiveness to MFs activation. We therefore investigated the AP waveform and properties in WT and PRRT2 KO GCs from acute cerebellar slices. Current-clamp GCs recordings in slices revealed a strong impact of PRRT2 deletion on the AP characteristics, in line with what observed in primary GCs. The AP overshoot was significantly increased in PRRT2 KO GCs when compared to WT GCs (Fig. 6A,B), while no significant differences in AP threshold and width were detected (Fig. 6C,D). PRRT2 KO GCs also showed a more biphasic behavior with a pronounced AIS component in the phase-plane plot analysis (Fig. 6E,F) described by a faster rising phase when compared to WT GCs (Fig. 6G,I). Furthermore, the somato-dendritic component (SD) of the AP was also positively modulated by the absence of PRRT2 as shown by the higher slope obtained in PRRT2 KO GCs (Fig. 6H,J). Taken together these data support a positive modulation of the activity of Na^+ channels located in the AIS and SD compartments of GCs in the absence of PRRT2.

3.7. Transient and persistent granule cell Na^+ currents are upregulated in PRRT2 KO cerebellar slices

In order to gain a better understanding of the molecular and functional mechanisms underlying GCs increased responsiveness to MF activation in PRRT2 KO mice, we investigated whether Na^+ currents were upregulated in acute cerebellar slices, as observed in GC primary cultures. Sodium currents were fully blocked by the bath application of TTX (1 μM) and were isolated by subtraction of the TTX-insensitive trace from the control trace. Transient Na^+ currents were elicited by depolarizing voltage steps lasting 20 ms and applied in 5-mV increments from −75 to 15 mV from a holding potential of −80 mV (Magistretti et al., 2006; Fig. 7A). Transient currents displayed significantly increased values in PRRT2 KO GCs, in the absence of appreciable shifts in the peak voltage (Fig. 7A,B). However, fitting the conductance versus voltage relationship to the Boltzmann equation showed comparable slopes and $V_{0.5}$ values of WT and PRRT2 KO transient Na^+ currents (Fig. 7C,D). Similarly, transient current inactivation curves revealed no significant differences under both tested conditions (Fig. 7E,F), pairing the data obtained on primary GCs.

The persistent Na^+ current is a hallmark of mature GCs and influences AP firing at just-threshold depolarization level (Magistretti et al., 2006). Since PRRT2 KO GCs displayed a higher intra-burst frequency than WT GCs (see Fig. 5C,D), we recorded persistent Na^+ currents from GCs in response to a 500-ms depolarization step from −75 to −40 mV (Fig. 7G). Due to the small amplitude of Na^+ currents, the signal-to-noise ratio was increased by averaging of 4–8 traces recorded at each tested potential. The long depolarization step elicited transient Na^+ currents that displayed an incomplete inactivation, revealing the persistent Na^+ current component. Strikingly, GCs from PRRT2 KO mice displayed a dramatic increase in persistent Na^+ currents (Fig. 7H). Furthermore, fitting the normalized conductance curves to the Boltzmann equation revealed a significant left shift of the curve that was paralleled by a more negative $V_{0.5}$ and a significant increase in the slope value in PRRT2 KO GCs with respect to WT GCs (Fig. 7I,J).

Resurgent Na^+ currents were also investigated in GCs using repolarizing pulses from −80 to −30 mV following a 20-ms pre-pulse to 0 mV (Fig. 7K). Although the peak of the resurgent current was higher in PRRT2 KO GCs, the amplitude of the resurgent current density at the net of the persistent Na^+ current (also increased in PRRT2 KO GCs) revealed no significant changes between WT and PRRT2 KO GCs (Fig. 7L).

4. Discussion

Paroxysmal kinesigenic dyskinesia is the most frequent phenotype of patients bearing loss-of-function PRRT2 mutations (Mir et al., 2005; Ebrahimi-Fakhari et al., 2015; Mo et al., 2019). However, whether PKD has a cortical or subcortical origin is still matter of debate. In the past, PKD was considered as a form of reflex epilepsy, given the paroxysmal nature of the attacks, its frequent clinical association with abnormal interictal EEG activities or overt epilepsy and excellent response to anticonvulsants (Mir et al., 2005; van Strien et al., 2012; Ebrahimi-Fakhari et al., 2015; Mo et al., 2019; Corradi et al., 2020). More recently, however, the participation of other brain areas involved in motor control, such as the basal ganglia and the cerebellum has been hypothesized, mostly on the basis of animal studies.

Although PRRT2 is widely expressed in several brain areas including cerebral cortex, basal ganglia and hippocampus, it reaches the highest expression levels in the cerebellum, specifically in GCs (Michetti et al., 2017a). Consistent with the physiological PRRT2 expression pattern, robust experimental evidence points to a major involvement of the cerebellum in the generation of the dyskinetic phenotype observed in patients bearing loss-of-function PRRT2 mutations and PRRT2 KO mice (Michetti et al., 2017a; Tan et al., 2018; Calame et al., 2020).

The cerebellum is a unique brain area devoted to the fine control of motor planning and execution. It is an efficient computational interface between motor intentionality and motor programming as well as between motor commands and sensory feedbacks that allows optimal motor planning and real-time optimization of ongoing movements (D'Angelo and Casali, 2013). Data obtained in the PRRT2 KO mouse have suggested that motor paroxysms primarily originate in the cerebellum, rather than in the basal ganglia-thalamic-cortical circuit and are associated with irregular PC activity (Tan et al., 2018). Purkinje cell firing dysfunctions play a key role in the generation of cerebellum-related behavioral alterations (Becker et al., 2014; Khan and Jinnah,

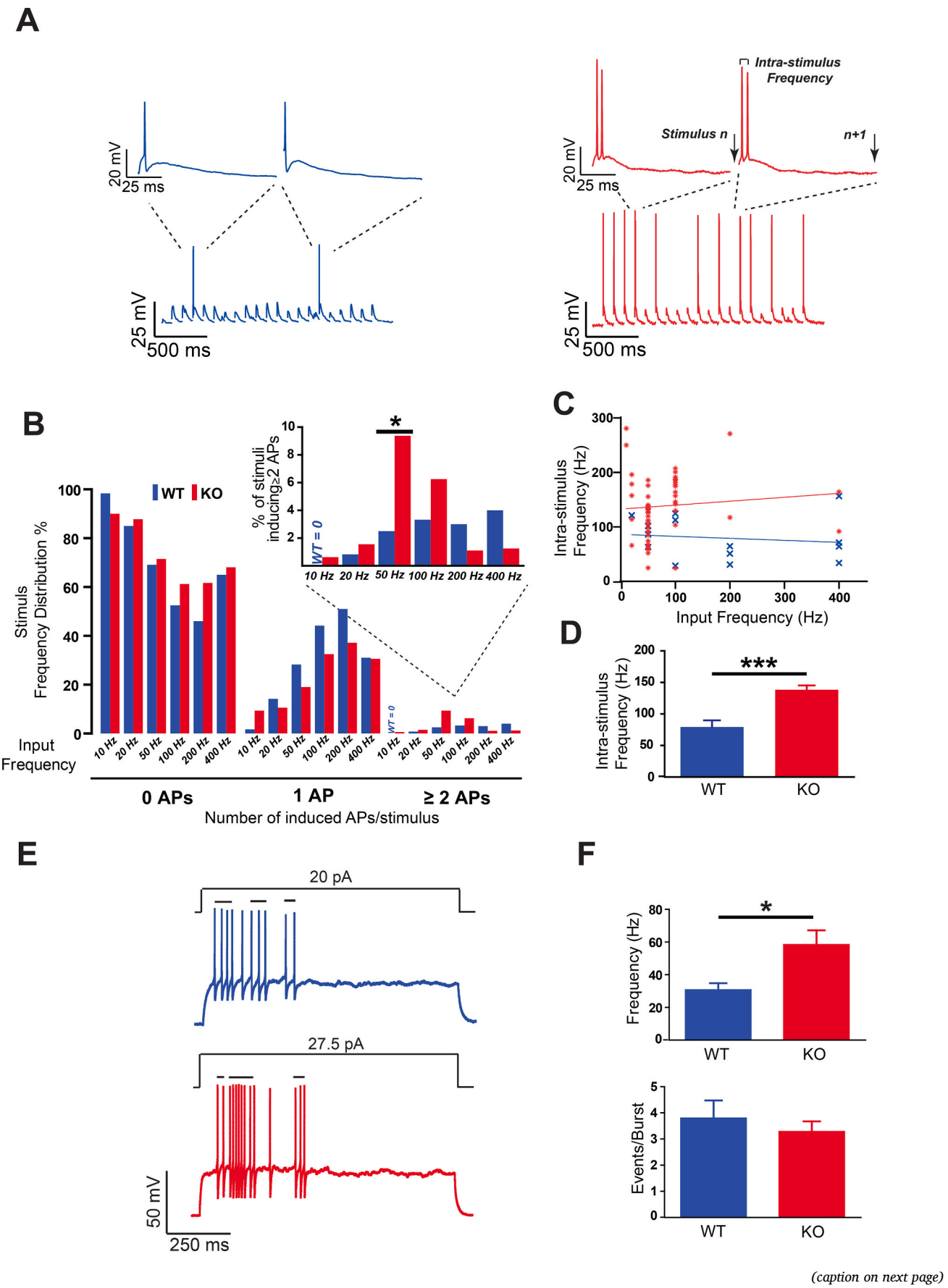

(caption on next page)

Fig. 5. Multiple action potential discharge profile of PRRT2 KO granule cells in acute cerebellar slices.
A-D. The propensity of GCs to discharge multiple APs upon MF stimulation was investigated by applying 20 stimuli at increasing input frequency (10–400 Hz). (A) Representative current-clamp traces recorded in WT and PRRT2 KO GCs in response to a 10-Hz train of 20 stimuli (stimulation artifacts were blanked for clarity). (B) Frequency distribution of the percentage of the total applied stimuli eliciting 0, 1 or 2 or more APs per stimulus. *Inset:* enlarged scale of the frequency distribution of the percentage of stimuli eliciting ≥2 APs per stimulus. The propensity of multiple AP discharges was higher in PRRT2 KO GCs (*red bars*) compared to WT (*blue bars*) GCs at most of input frequencies, reaching a significance at 50 Hz. *p < 0.05; Fisher's exact test. (C) MFinput frequency stimulation does not influence multiple discharges of APs. MF input frequency stimulation plotted versus the frequency of multiple AP discharges (≥ 2 APs per stimulus) reveals no correlation in both WT (Pearson's correlation coefficient $r = 0.139$; $p = 0.6347$) and PRRT2 KO (Pearson's correlation coefficient $r = 0.094$, $p = 0.4659$) GCs. (D) The intra-stimulation frequency of multiple AP discharges was significantly higher in mutant (*red bar; n* = 61) as compared to WT (*blue bar; n* = 14) GCs. ***p < 0.001; unpaired Student's *t*-test. E,F. Just-threshold bursting properties were investigated in PRRT2 KO (red traces/bars) and WT (blue traces/bars) GCs. (E) Representative current-clamp recordings of evoked firing. Horizontal lines represent detected bursts. (F) Mean (± sem) firing frequency (*upper panel*) and APs/burst (*lower panel*) for both phenotypes (WT, n = 20; PRRT2 KO, *n* = 28). While no differences were found in the number of APs discharged/burst (WT: 3.8 ± 0.67, n = 20; PRRT2 KO: 3.29 ± 0.39, n = 28; mean ± sem, $p = 0.4477$), the intra-burst frequency was significantly higher in PRRT2 KO GCs compared to WT GCs (WT: 30.79 ± 4.03 Hz, n = 20; KO: 58.45 ± 8.7 Hz, n = 28; mean ± SEM, $p = 0.0077$). *p < 0.05; Mann-Whitney's *U* test.

2002; Isaksen et al., 2017; Matsushita et al., 2002). The simple spike firing pattern of PCs is enhanced by GC parallel fibers making excitatory synapses in the dendritic tree of PCs in the molecular layer. Cerebellar GCs represent half of total brain neurons and act as the entry gate and distribution station for the vast cerebellar inputs brought to PCs by MFs. PC in turn inhibit the output neurons of the deep cerebellar nuclei (DCN) that activate the thalamus and its connections with the cerebral cortex and the striatum to contribute to motor planning and execution (Chen et al., 2014). Moreover, the axons of DCN neurons project recurrent nucleo-cortical fibers that activate GCs, constituting an internal amplification mechanism that provides a closed-loop sustained activation of GCs and PCs thought to be important in motor learning (Gao et al., 2016).

Interestingly, synaptic transmission at MF-GCs synapses was not affected by PRRT2 deletion, in contrast with the synaptic phenotype observed in hippocampal and neocortical synapses (Valente et al., 2016a and 2019; Michetti et al., 2017a). It is conceivable that the absence of a synaptic phenotype depends on the scarce or absent expression of PRRT2 in the pontine pre-cerebellar nuclei (pontine nucleus and *nucleus reticularis tegmenti pontis;* Sillitoe et al., 2012) projecting to the GCs of lobule VI, as recently shown with β-gal staining in heterozygous PRRT2 KO mice (Michetti et al., 2017a). Indeed, the absence of PRRT2-expressing projections to lobule VI allowed us to monitor the GC behavior in the absence of confounding effects in synaptic transmission and plasticity at the MF-GC synapses.

4.1. *PRRT2 negatively controls Na^+ currents and intrinsic excitability of cerebellar granule cells under physiological conditions*

Given the very high expression level in GCs, we hypothesized that the dyskinetic phenotype caused by PRRT2 deficiency and the irregular and bursting PC activity is due to a dysfunction of GCs. Using the PRRT2 KO mouse that we were the first to characterize (Michetti et al., 2017a), we demonstrate that: (i) primary cerebellar GCs display enhanced Na^+ current density due to an increased expression of Na^+ channels, in the absence of changes in their biophysical properties; (ii) primary cerebellar GCs are markedly hyperexcitable and display an increased length of the AIS that is more proximal to the soma; (iii) GCs in cerebellar slices display an increased firing responsiveness to MF activation, with a marked propensity to fire multiple APs characterized by enhanced AIS and SD components, in the absence of substantial changes in the MF/GC synaptic transmission; (iv) the hyperexcitability phenotype of GCs in cerebellar slices is correlated with an increase amplitude of both transient and persistent Na^+ currents.

The persistent Na^+ current is a subthreshold non-inactivating voltage-dependent current expressed in several neuronal types with a pronounced slow inactivation and J/V peak and activation curve shifted toward hyperpolarized potentials (Magistretti et al., 2006; Lewis and Raman, 2014; Ceballos et al., 2017). The persistent Na^+ current flows through the same channels as transient and resurgent Na^+ currents. In spite of the small amplitude, the persistent Na^+ current can have a major impact on membrane excitability, particularly in small neurons with high R_{in} like mature cerebellar GCs. Indeed, they have been reported to increase the rate at which the GC membrane potential approaches firing threshold, to boost near-threshold depolarization and producing spontaneous firing (D'Angelo et al., 1998).

The persistent Na^+ current in cerebellar PCs and GCs has been associated with the $Na_V1.6$ α-subunit and its binding to the $Na_V\beta4$ subunit. Previous studies have shown that the persistent Na^+ current is reduced in neurons from mice lacking the $Na_V1.6$ α subunit (Aman and Raman, 2007). Moreover, knockdown of the $Na_V\beta4$ subunit in cerebellar GCs reduced the persistent currents, without affecting Na^+ transient current, decreasing repetitive firing (Bant and Raman, 2010). Interestingly, the observation that mutations in Na_V subunits that increase the expression of persistent Na^+ current are associated with paroxysmal disorders, such as epilepsy (Stafstrom, 2007), is highly suggestive for a key role of this phenotype in the pathogenesis of PRRT2 movement disorders.

Recently, PRRT2 was shown to interact and downregulate $Na_V1.2$/1.6 channel expression, so that loss-of-function of PRRT2 leads to increased Na^+ currents and hyperexcitability in excitatory neurons (Fruscione et al., 2018). Interestingly, gain-of-function mutations in SCN8A encoding Nav1.6 channels cause very similar diseases with excellent response to Na^+ channel blockers (Gardella et al., 2016). These results prove that GC Na^+ channels are the fundamental cerebellar target of PRRT2-deficiency and play a key role in the dyskinetic phenotype of PRRT2 KO mice and PRRT2 patients. The marked changes in GC excitability and GC/PF to PC transmission caused by the genetic ablation of PRRT2 may lead to the highly irregular cerebellar cortical and nuclear output that can be maintained by the reverberant DCN-GC connections, thus generating and prolonging the dyskinetic attacks. Interestingly, PRRT2 can play an opposite role with respect to fibroblast growth factor homologous factors (FHFs), a family of voltage-gated Na^+ channel binding proteins. Indeed, lack of FHFs decreases GC excitability, increases voltage threshold for spike initiation at the AIS and causes ataxia and motor weakness (Goldfarb et al., 2007; Dover et al., 2016).

4.2. *A combined synapto/chanellopathy at cerebellar granule neurons and PF-PC synapses at the basis of the paroxysmal dyskinetic phenotype associated with PRRT2 loss-of-function*

Shared phenotypes exist between PRRT2-linked PKD and other cerebellar chanellopathies. Mutations in genes encoding Ca^{2+} channels or Ca^{2+} channel interactors have been associated with recurrent paroxysmal disorders in man and mouse. The dyskinetic/ataxic mice *tottering, lethargic, rolling* and *moonwalker* bearing mutations in Cav2.1, Cav2.1β4 and TRPC3 (Becker et al., 2014; Khan and Jinnah, 2002; Matsushita et al., 2002) share paroxysmal phenotypic traits with the PRRT2 KO mouse (Michetti et al., 2017a; Tan et al., 2018).

We and others have shown that PRRT2 is an important catalyst of the Ca^{2+}-evoked neurotransmitter release machinery at the synapse (Valente et al., 2016a; Coleman et al., 2018). Through its interactions with

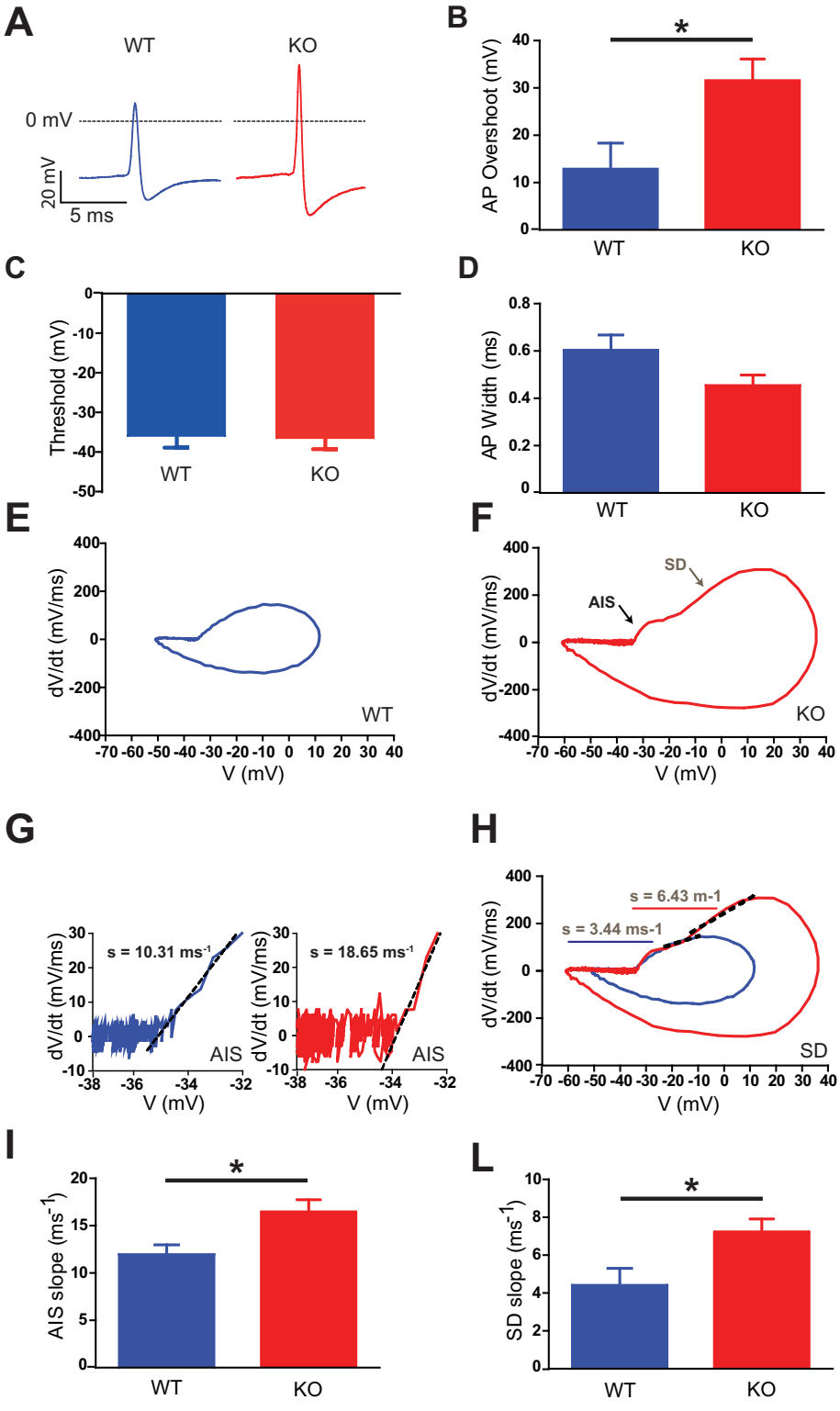

Fig. 6. Action potential properties in PRRT2 KO granule cells in acute cerebellar slices.
Action potential waveform and properties were studied in PRRT2 KO (red traces/bars) and WT (blue traces/bars) GCs. A. Representative current-clamp recordings of evoked APs. B—D. Mean (± sem) AP overshoot (B), threshold voltage (C) and half-width (D). WT, $n = 8$; PRRT2 KO, $n = 14$. *E*-H. Representative phase-plot analysis of AP waveforms in WT (E) and PRRT2 KO (F) GCs. The analysis of the slopes for the AIS (G) and somato-dendritic (SD; H) components of the AP revealed increased slope values in mutant GCs for both components. I,J. Means (± sem) values of AIS (I) and SD slopes (J) reveal more pronounced AIS and SD components in mutant GCs compared to WT GCs. WT, n = 8; KO, n = 14. *p < 0.05; unpaired Student's *t*-test.

SNARE proteins and synaptotagmin, PRRT2 endows the SNARE complex with Ca^{2+} sensitivity and boost the release probability in response to the AP. In the absence of PRRT2, the reduction of release probability triggers a marked synaptic facilitation in response to high-frequency stimulation that, by high-pass filtering of input synaptic signals, contributes to the hyperexcitability phenotype (Valente et al., 2016a; Fruscione e al., 2018; Valente et al., 2019). This phenotype, initially observed in primary neurons, was subsequently confirmed at the level of PF-PC synapses in the cerebellar cortex, where PRRT2 deletion induced a long-lasting facilitation and inhibited the expression of synaptic depression (Michetti et al., 2017a). Thus, the physiological role of PRRT2 at the synaptic level could be that of stabilizing and increasing the reliability of basal transmission. In this respect, PRRT2 can be considered a network stability gene, acting as a lowpass filter on network activity (Jackman and Regehr, 2017; Michetti et al., 2017b). While a pronounced synaptic facilitation phenotype was also observed

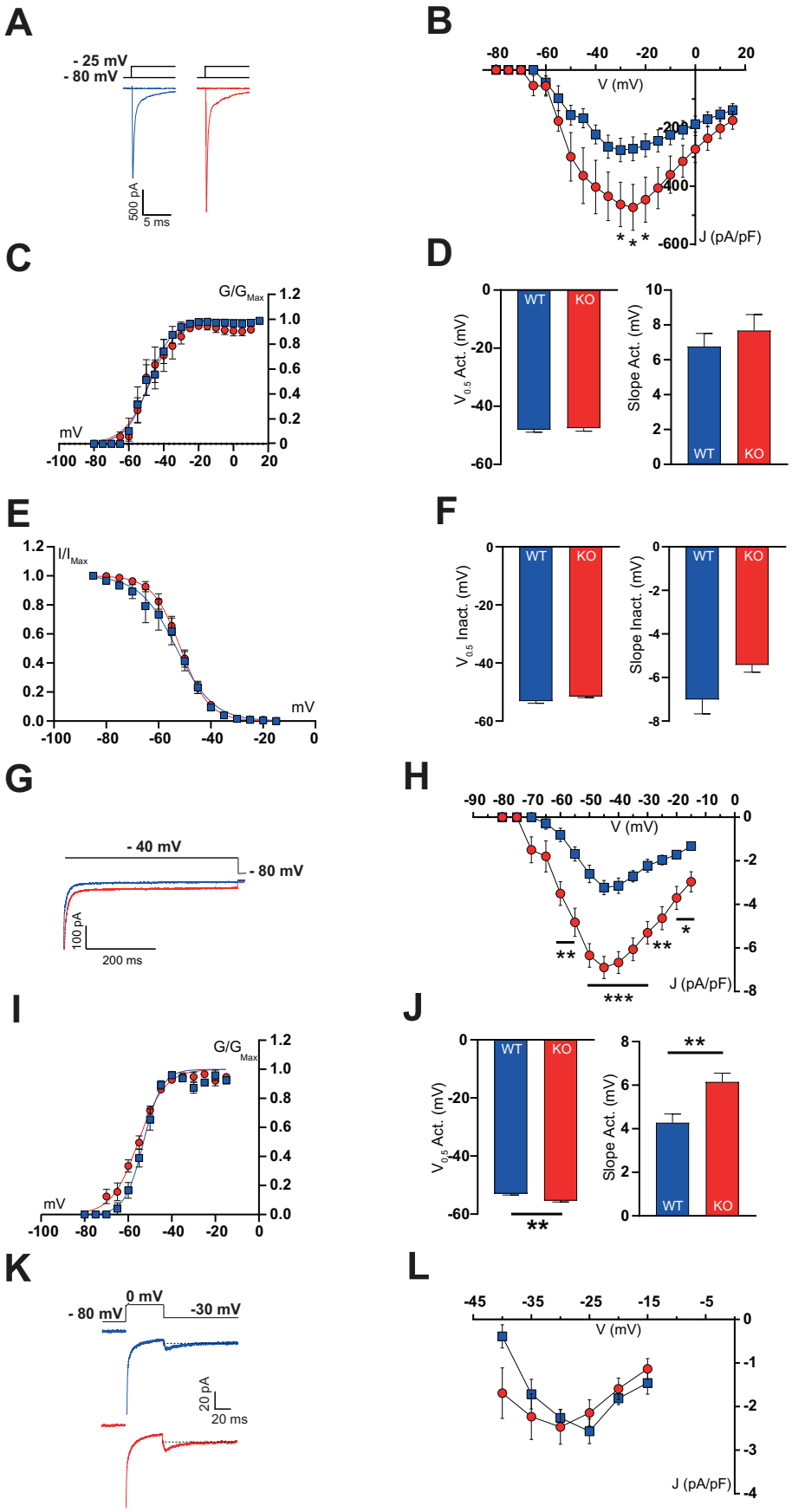

Fig. 7. PRRT2 deletion increases transient and persistent, but not resurgent, Na^+ currents in granule cells from acute cerebellar slices.

A-F. Transient Na^+ current. Representative recordings (A) and J/V relationships (B) reveal a significant increase of transient Na^+ currents in mutant GCs (red traces/symbols) with respect to WT GCs (blue traces/symbols). The analysis of Na^+ channel activation properties by fitting the activation curve to the Boltzmann equation (C) reveals no significant changes in the half-maximal activation potential ($V_{0.5}$) and slope in WT and PRRT2 KO GCs (D). The analysis of the inactivation curves of transient Na^+ currents (E) did not detect genotype-dependent differences in the slope of inactivation or in the half-maximal inactivation potential ($V_{0.5}$; F). Mean (± sem) capacitance: WT, 4.37 ± 0.69; PRRT2 KO, 4.10 ± 0.484. WT, n = 8; PRRT2 KO, n = 7; *p < 0.05; unpaired Student's *t*-test/Mann-Whitney's *U* test.

G-J. Persistent Na^+ currents. Representative recordings (G) and J/V relationships (H). The persistent Na^+ currents were markedly increased in PRRT2 KO GCs (red traces/symbols) when compared to WT GCs (blue traces/symbols). Boltzmann fitting of the activation curve of PRRT2 KO GCs (I) revealed a hyperpolarization shift of the $V_{0.5}$ value and an increased slope compared to WT (J). Mean (± sem) capacitance: WT, 3.89 ± 0.71; PRRT2 KO, 3.78 ± 0.34. WT, $n = 5$; KO, n = 7; *p < 0.05, **p < 0.01, ***p < 0.001; unpaired Student's *t*-test/Mann-Whitney's *U* test.

K,L. Resurgent Na^+ currents. Representative averaged traces (K) and J/V relationships (L). The J/V analysis of the resurgent Na^+ currents revealed no significant differences resurgent Na^+ currents across genotypes at the net of the persistent Na^+ current. Mean (± sem) capacitance: WT, 3,60 ± 0.32; PRRT2 KO, 4.28 ± 0.22. WT, $n = 4$; PRRT2 KO, $n = 5$.

at the PF/PC synapses in cerebellar slices of PRRT2 KO mice by us and others (Michetti et al., 2017a, 2017b; Tan et al., 2018), the glutamatergic input at the MF/GC synapses was not altered by PRRT2 KO cerebellar slices. The lack of a synaptic phenotype in the MF/PC synapses, while emphasizing the central role of GC's intrinsic excitability in the cerebellar phenotype of PRRT2 KO mice, indicates that the synaptic involvement under conditions of PRRT2 deficiency largely depends on the expression level and synaptic targeting of PRRT2 in specific neuronal systems.

A similar phenotype, paroxysmal non-kinesigenic dyskinesia, was identified in patients and knockout mice for PNKD, a novel synaptic protein that interacts with RIM1 and RIM2 at presynaptic terminals known to facilitate neurotransmitter release (Shen et al., 2015). From these considerations, it is conceivable that paroxysmal movement disorders can result from mutations either in ion channels/ion channel accessory proteins or in proteins regulating the probability of release and thereby the short-term plasticity/filtering properties of synaptic connections. In the case of PRRT2 deficiency, both mechanisms can contribute to the pathology, generating a hybrid synapto/chanellopathy that profoundly alters cerebellar function in motor control.

5. Conclusions

In conclusion, the results reveal the potential involvement of the cerebellum in forms of paroxysmal disorders. While the distinct roles played by PRRT2 at synaptic and AIS levels may explain the pleiotropic phenotypic expression of the PRRT2-linked diseases and the substantial lack of genotype/phenotype correlations (Heron and Dibbens, 2013; Valtorta et al., 2016), PRRT2 may be concomitantly acting at both levels, simultaneously affecting intrinsic excitability and short-term synaptic plasticity. Indeed, synaptic facilitation is triggered by high-frequency activity that can result from an increase in intrinsic excitability in response to physiological inputs. Thus, the two mechanisms can synergistically participate in the emergence of the PRRT2-linked paroxysms, as recently suggested by neural network modelling studies (Valente et a., 2019).

Funding

The study was supported by research grants from European Union EraNet Neuron 2017 SNAREopathies (to FaBe); Compagnia di San Paolo Torino (2015.0546 to FaBe and 2017.20612 to PB); IRCCS Ospedale Policlinico San Martino (Ricerca Corrente and "5 × 1000" to PV and FaBe) and Italian Ministry of University and Research (PRIN 2015-H4K2CR and 2017-A9MK4R to FaBe). The support of Telethon-Italy (Grant GGP19120 to FaBe) is also acknowledged.

Author contributions

FrBi and PV designed and performed the electrophysiological experiments in slices and cultures respectively, and analyzed the data, AM performed the immunocytochemical experiments and the morphometric analysis of the AIS. PB supervised the electrophysiology and immunocytochemical experiments and participated in data analysis and interpretation. All authors participated in discussing the data, preparing the figures and writing parts of the manuscript. FaBe supervised the research, discussed the data and wrote the manuscript.

Declaration of Competing Interest

The authors have no competing financial interests to declare.

Acknowledgements

We thank Drs. Teresa Soda, Francesca Prestori and Prof. Egidio D'Angelo (University of Pavia, Pavia, Italy) for training in ex vivo GC recordings. We thank dr. Silvia Casagrande (Department Experimental Medicine, University of Genova) for help in the preparation of primary cultures of GCs. We also thank Drs. Caterina Michetti, Riccardo Navone and Diego Moruzzo (Istituto Italiano di Tecnologia, Genova, Italy) for their help in the maintenance, breeding and genotyping of the PRRT2 mouse strain and Prof. Egidio D'angelo for critical reading of the manuscript.

Appendix A. Supplementary data

Supplementary data to this article can be found online at https://doi.org/10.1016/j.nbd.2021.105275.

References

Afshari, F.S., Ptak, K., Khaliq, Z.M., Grieco, T.M., Slater, N.T., McCrimmon, D.R., Raman, I.M., 2004. Resurgent Na currents in four classes of neurons of the cerebellum. J. Neurophysiol. 92, 2831–2843.
Aman, T.K., Raman, I.M., 2007. Subunit dependence of Na^+ channel slow inactivation and open channel block in cerebellar neurons. Biophys. J. 92, 1938–1951.
Bant, J.S., Raman, I.M., 2010. Control of transient, resurgent, and persistent current by open-channel block by Na channel β4 in cultured cerebellar granule neurons. Proc. Natl. Acad. Sci. U. S. A. 107, 12357–12362.
Becker, E.B.E., 2014. The Moonwalker mouse: new insights into TRPC3 function, cerebellar development, and ataxia. Cerebellum 13, 628–636.
Calame, D.J., Xiao, J., Khan, M.M., Hollingsworth, T.J., Xue, Y., Person, A.L., LeDoux, M. S., 2020. Presynaptic PRRT2 deficiency causes cerebellar dysfunction and paroxysmal kinesigenic dyskinesia. Neuroscience S0306-4522 (30559–30555).
Ceballos, C.C., Roque, A.C., Leão, R.M., 2017. A negative slope conductance of the persistent sodium current prolongs subthreshold depolarizations. Biophys. J. 113, 2207–2217.
Chen, W.-J., Lin, Y., Xiong, Z.-Q., Wei, W., Ni, W., Tan, G.-H., Guo, S.-L., He, J., Chen, Y.-F., Zhang, Q.-J., Li, H.-F., Lin, Y., Murong, S.-X., Xu, J., Wang, N., Wu, Z.-Y., 2011. Exome sequencing identifies truncating mutations in PRRT2 that cause paroxysmal kinesigenic dyskinesia. Nat. Genet. 43, 1252–1255.
Chen, C.H., Fremont, R., Arteaga-Bracho, E.E., Khodakhah, K., 2014. Short latency cerebellar modulation of the basal ganglia. Nat. Neurosci. 17, 1767–1775.
Coleman, J., Jouannot, O., Ramakrishnan, S.K., Zanetti, M.N., Wang, J., Salpietro, V., Houlden, H., Rothman, J.E., Krishnakumar, S.S., 2018. PRRT2 regulates synaptic fusion by directly modulating SNARE complex assembly. Cell Rep. 22, 820–831.
Cook, A.A., Fields, E., Watt, A.J., 2020. Losing the beat: contribution of Purkinje cell firing dysfunction to disease, and its reversal. Neuroscience S0306-4522, 30377–30378.
Corradi, A., Valente, P., Michetti, C., Benfenati, F., 2020. Pathophysiology of paroxysmal dyskinesia. In: Sethi, K.D., Erro, R., Bhatia, K.P. (Eds.), Paroxysmal Movement Disorders. Springer Nature, Switzerland, pp. 95–108.
D'Angelo, E., Casali, S., 2013. Seeking a unified framework for cerebellar function and dysfunction: from circuit operations to cognition. Front. Neural Circuits 6, 116.
D'Angelo, E., De Filippi, G., Rossi, P., Taglietti, V., 1998. Ionic mechanism of electroresponsiveness in cerebellar granule cells implicates the action of persistent sodium current. J. Neurophysiol. 80, 493–503. Aug.
D'Angelo, E., Nieus, T., Maffei, A., Armano, S., Rossi, P., Taglietti, V., Fontana, A., Naldi, G., 2001. Theta-frequency bursting and resonance in cerebellar granule cells: experimental evidence and modeling of a slow K^+-dependent mechanism. J. Neurosci. 21, 759–770.
Dover, K., Marra, C., Solinas, S., Popovic, M., Subramaniyam, S., Zecevic, D., D'Angelo, E., Goldfarb, M., 2016. FHF-independent conduction of action potentials along the leak-resistant cerebellar granule cell axon. Nat. Commun. 7, 12895.
Ebrahimi-Fakhari, D., Saffari, A., Westenberger, A., Klein, C., 2015. The evolving spectrum of PRRT2-associated paroxysmal diseases. Brain 138, 3476–3495.
Fremont, R., Calderon, D.P., Maleki, S., Khodakhah, K., 2014. Abnormal high-frequency burst firing of cerebellar neurons in rapid-onset dystonia-parkinsonism. J. Neurosci. 34, 11723–11732.
Fruscione, F., Valente, P., Sterlini, B., Romei, A., Baldassari, S., Fadda, M., Prestigio, C., Giansante, G., Sartorelli, J., Rossi, P., Rubio, A., Gambardella, A., Nieus, T., Broccoli, V., Fassio, A., Baldelli, P., Corradi, A., Zara, F., Benfenati, F., 2018. PRRT2 controls neuronal excitability by negatively modulating Na^+ channel 1.2/1.6 activity. Brain 141, 1000–1016.
Gao, Z., Proietti-Onori, M., Lin, Z., Ten Brinke, M.M., Boele, H.J., Potters, J.W., Ruigrok, T.J., Hoebeek, F.E., De Zeeuw, C.I., 2016. Excitatory cerebellar nucleocortical circuit provides internal amplification during associative conditioning. Neuron 89, 645–657.
Gardella, E., Becker, F., Møller, R.S., Schubert, J., Lemke, J.R., Larsen, L.H., Eiberg, H., Nothnagel, M., Thiele, H., Altmüller, J., Syrbe, S., Merkenschlager, A., Bast, T., Steinhoff, B., Nürnberg, P., Mang, Y., Bakke Møller, L., Gellert, P., Heron, S.E., Dibbens, L.M., Weckhuysen, S., Dahl, H.A., Biskup, S., Tommerup, N., Hjalgrim, H., Lerche, H., Beniczky, S., Weber, Y.G., 2016. Benign infantile seizures and paroxysmal dyskinesia caused by and SCN8A mutation. Ann. Neurol. 79, 428–436.
Goldfarb, M., Schoorlemmer, J., Williams, A., Diwakar, S., Huang, X., Giza, J., Tchetchik, D., Kelley, K., Vega, A., Matthews, G., Rossi, P., Ornitz, D., D'Angelo, E., 2007. Fibroblast growth factor homologous factors control neuronal excitability through modulation of voltage gated sodium channels. Neuron 55, 449–463.

Grubb, M.S., Burrone, J., 2010. Activity-dependent relocation of the axon initial segment fine-tunes neuronal excitability. Nature 465, 1070–1074.
Heron, S.E., Dibbens, L.M., 2013. Role of PRRT2 in common paroxysmal neurological disorders: a gene with remarkable pleiotropy. J. Med. Genet. 50, 133–139.
Isaksen, T.J., Kros, L., Vedovato, N., Holm, T.H., Vitenzon, A., Gadsby, D.C., Khodakhah, K., Lykke-Hartmann, K., 2017. Hypothermia-induced dystonia and abnormal cerebellar activity in a mouse model with a single disease-mutation in the sodium-potassium pump. PLoS Genet. 13, e1006763.
Jackman, S.L., Regehr, W.G., 2017. The mechanisms and functions of synaptic facilitation. Neuron 94, 447–464.
Khan, Z., Jinnah, H.A., 2002. Paroxysmal dyskinesias in the lethargic mouse mutant. J. Neurosci. 22, 8193–8200.
Kross, L., De Zeeuw, C.I., 2018. PRRT2-dependent dyskinesia: cerebellar, paroxysmal and persistent. Cell Res. 28, 3–4.
Lee, H.Y., Greene, L.A., Mason, C.A., Manzini, M.C., 2009. Isolation and culture of post-natal mouse cerebellar granule neuron progenitor cells and neurons. JoVE 23. http://www.jove.com/index/Details.stp?ID=990.
Lee, H.Y., Huang, Y., Bruneau, N., Roll, P., Roberson, E.D., Hermann, M., Quinn, E., Maas, J., Edwards, R., Ashizawa, T., Baykan, B., Bhatia, K., Bressman, S., Bruno, M. K., Brunt, E.R., Caraballo, R., Echenne, B., Fejerman, N., Frucht, S., Gurnett, C.A., Hirsch, E., Houlden, H., Jankovic, J., Lee, W.L., Lynch, D.R., Mohammed, S., Müller, U., Nespeca, M.P., Renner, D., Rochette, J., Rudolf, G., Saiki, S., Soong, B.W., Swoboda, K.J., Tucker, S., Wood, N., Hanna, M., Bowcock, A.M., Szepetowski, P., Fu, Y.H., Ptáček, L.J., 2012. Mutations in the gene PRRT2 cause paroxysmal kinesigenic dyskinesia with infantile convulsions. Cell Rep. 1, 2–12.
Lerche, H., 2018. Synaptic or ion channel modifier? PRRT2 is a chameleon-like regulator of neuronal excitability. Brain 141, 938–941.
Lewis, A.H., Raman, I.M., 2014. Resurgent current of voltage-gated Na^+ channels. J. Physiol. 592, 4825–4838.
Liu, Y.-T., Nian, F.-S., Chou, W.-J., Tai, C.-Y., Kwan, S.-Y., Chen, C., Kuo, P.-W., Lin, P.-H., Chen, C.-Y., Huang, C.-W., Lee, Y.-C., Soong, B.-W., Tsai, J.-W., 2016. PRRT2 mutations lead to neuronal dysfunction and neurodevelopmental defects. Oncotarget 7, 39184–39196.
Magistretti, J., Castelli, L., Forti, L., D'Angelo, E., 2006. Kinetic and functional analysis of transient, persistent and resurgent sodium currents in rat cerebellar granule cells in situ: an electrophysiological and modelling study. J. Physiol. 573, 83–106.
Matsushita, K., Wakamori, M., Rhyu, I.J., Arii, T., Oda, S.-I., Mori, Y., Imoto, K., 2002. Bidirectional alterations in cerebellar synaptic transmission of tottering and rolling Ca^{2+} channel mutant mice. J. Neurosci. 22, 4388–4398.
Michetti, C., Castroflorio, E., Marchionni, I., Forte, N., Sterlini, B., Binda, F., Fruscione, F., Baldelli, P., Valtorta, F., Zara, F., Corradi, A., Benfenati, F., 2017a. The PRRT2 knockout mouse recapitulates the neurological diseases associated with PRRT2 mutations. Neurobiol. Dis. 99, 66–83.
Michetti, C., Corradi, A., Benfenati, F., 2017b. PRRT2, a network stability gene. Oncotarget 8, 55770–55771.
Mir, P., Huang, Y.-Z., Gilio, F., Edwards, M.J., Berardelli, A., Rothwell, J.C., Bhatia, K.P., 2005. Abnormal cortical and spinal inhibition in paroxysmal kinesigenic dyskinesia. Brain 128, 291–299.
Mo, J., Wang, B., Zhu, X., Wu, X., Liu, Y., 2019. PRRT2 deficiency induces paroxysmal kinesigenic dyskinesia by influencing synaptic function in the primary motor cortex of rats. Neurobiol. Dis. 121, 274–285.
Neychev, V.K., Fan, X., Mitev, V.I., Hess, E.J., Jinnah, H.A., 2008. The basal ganglia and cerebellum interact in the expression of dystonic movement. Brain 131, 2499–2509.
Osorio, N., Alcaraz, G., Padilla, F., Couraud, F., Delmas, P., Crest, M., 2005. Differential targeting and functional specialization of sodium channels in cultured cerebellar granule cells. J. Physiol. 569, 801–816.
Osorio, N., Cathala, L., Meisler, M.H., Crest, M., Magistretti, J., Delmas, P., 2010. Persistent $Na_V1.6$ current at axon initial segments tunes spike timing of cerebellar granule cells. J. Physiol. 588, 651–670.
Prestigio, C., Ferrante, D., Valente, P., Casagrande, S., Albanesi, E., Yanagawa, Y., Benfenati, F., Baldelli, P., 2019. Spike-related electrophysiological identification of cultured hippocampal excitatory and inhibitory neurons. Mol. Neurobiol. 56, 6276–6292.
Rancz, E.A., Ishikawa, T., Duguid, I., Chadderton, P., Mahon, S., Häusser, M., 2007. High-fidelity transmission of sensory information by single cerebellar mossy fibre boutons. Nature 450, 1245–1248.
Rossi, P., Sterlini, B., Castroflorio, E., Marte, A., Onofri, F., Valtorta, F., Maragliano, L., Corradi, A., Benfenati, F., 2016. A novel topology of proline-rich transmembrane protein 2 (PRRT2): hints for an intracellular function at the synapse. J. Biol. Chem. 291, 6111–6123.
Savino, E., Cervigni, R.I., Povolo, M., Stefanetti, A., Ferrante, D., Valente, P., Corradi, A., Benfenati, F., Guarnieri, F.C., Valtorta, F., 2020. Proline-rich transmembrane protein 2 (PRRT2) regulates the actin cytoskeleton during synaptogenesis. Cell Death Dis. 11, 856.
Shen, Y., Ge, W.-P., Li, Y., Hirano, A., Lee, H.-Y., Rohlmann, A., Missler, M., Tsien, R.W., Jan, L.Y., Fu, Y.-H., Ptáček, L.J., 2015. Protein mutated in paroxysmal dyskinesia interacts with the active zone protein RIM and suppresses synaptic vesicle exocytosis. Proc. Natl. Acad. Sci. U. S. A. 112, 2935–2941.
Sillitoe, R.V., Fu, Y.H., Watson, C., 2012. Cerebellum. In: The Mouse Nervous System. Elsevier, pp. 360–397.
Silver, R.A., Cull-Candy, S.G., Takahashi, T., 1996. Non-NMDA glutamate receptor occupancy and open probability at a rat cerebellar synapse with single and multiple release sites. J. Physiol. 494, 231–250.
Skarnes, W.C., Rosen, B., West, A.P., Koutsourakis, M., Bushell, W., Iyer, V., Mujica, A.O., Thomas, M., Harrow, J., Cox, T., Jackson, D., Severin, J., Biggs, P., Fu, J., Nefedov, M., de Jong, P.J., Stewart, A.F., Bradley, A., 2011. A conditional knockout resource for the genome-wide study of mouse gene function. Nature 474, 337–342.
Sola, E., Prestori, F., Rossi, P., Taglietti, V., D'Angelo, E., 2004. Increased neurotransmitter release during long-term potentiation at mossy fibre-granule cell synapses in rat cerebellum. J. Physiol. 557, 843–861.
Stafstrom, C.E., 2007. Persistent sodium current and its role in epilepsy. Epilepsy Curr. 7, 15–22.
Tan, G.-H., Liu, Y.-Y., Wang, L., Li, K., Zhang, Z.-Q., Li, H.-F., Yang, Z.-F., Li, Y., Li, D., Wu, M.-Y., Yu, C.-L., Long, J.-J., Chen, R.-C., Li, L.-X., Yin, L.-P., Liu, J.-W., Cheng, X.-W., Shen, Q., Shu, Y.-S., Sakimura, K., Liao, L.-J., Ying Wu, Z.-Y., Xiong, Z.-Q., 2018. PRRT2 deficiency induces paroxysmal kinesigenic dyskinesia by regulating synaptic transmission in cerebellum. Cell Res. 28, 90–110.
Tsai, M.H., Nian, F.S., Hsu, M.H., Liu, W.S., Liu, Y.T., Liu, C., Lin, P.H., Hwang, D.Y., Chuang, Y.C., Tsai, J.W., 2019. PRRT2 missense mutations cluster near C-terminus and frequently lead to protein mislocalization. Epilepsia 60, 807–817.
Valente, P., Castroflorio, E., Rossi, P., Fadda, M., Sterlini, B., Cervigni, R.I., Prestigio, C., Giovedì, S., Onofri, F., Mura, E., Guarnieri, F.C., Marte, A., Orlando, M., Zara, F., Fassio, A., Valtorta, F., Baldelli, P., Corradi, A., Benfenati, F., 2016a. PRRT2 is a key component of the Ca^{2+}-dependent neurotransmitter release machinery. Cell Rep. 15, 117–131.
Valente, P., Orlando, M., Raimondi, A., Benfenati, F., Baldelli, P., 2016b. Fine tuning of synaptic plasticity and filtering by GABA released from hippocampal autaptic granule cells. Cereb. Cortex 26, 1149–1167.
Valente, P., Romei, A., Fadda, M., Sterlini, B., Lonardoni, D., Forte, N., Fruscione, F., Castroflorio, E., Michetti, C., Giansante, G., Valtorta, F., Tsai, J.-W., Zara, F., Nieus, T., Corradi, A., Fassio, A., Baldelli, P., Benfenati, F., 2019. Constitutive inactivation of the PRRT2 gene alters short-term synaptic plasticity and promotes network hyperexcitability in hippocampal neurons. Cereb. Cortex 29, 2010–2033.
Valtorta, F., Benfenati, F., Zara, F., Meldolesi, J., 2016. PRRT2: from paroxysmal disorders to regulation of synaptic function. Trends Neurosci. 39, 668–679.
van Strien, T.W., van Rootselaar, A.F., Hilgevoord, A.A., Linssen, W.H., Groffen, A.J., Tijssen, M.A., 2012. Paroxysmal kinesigenic dyskinesia: cortical or non-cortical origin. Parkinsonism Relat. Disord. 18, 645–648.
Xu-Friedman, M.A., Regehr, W.G., 2003. Ultrastructural contributions to desensitization at cerebellar mossy fiber to granule cell synapses. J. Neurosci. 23, 2182–2192.